Arrow shaped elasto-inertial rotating waves

Journal:	*Philosophical Transactions A*
Manuscript ID	RSTA-2022-0227.R2
Article Type:	Research
Date Submitted by the Author:	n/a
Complete List of Authors:	Lopez, Jose Manuel; Polytechnic University of Catalonia, Physics Altmeyer, Sebastian; Universitat Politecnica de Catalunya, Physics
Issue Code (this should have already been entered and appear below the blue box, but please contact the Editorial Office if it is not present):	TAYLOR
Subject:	Fluid mechanics < PHYSICS, Computational physics < COMPUTER SCIENCE, Computer modelling and simulation < COMPUTER SCIENCE, Computational mechanics < COMPUTER SCIENCE, Applied mathematics < MATHEMATICS, Complexity < PHYSICS
Keywords:	Taylor-Couette flow, visco-elastic fluid, rotating waves, instability, bifurcations

SCHOLARONE™
Manuscripts

1
2
3
4
5
6
7
8
9
10
11
12
13
14
15
16
17
18
19
20
21
22
23
24
25
26
27
28
29
30
31
32
33
34
35
36
37
38
39
40
41
42
43
44
45
46
47
48
49
50
51
52
53
54
55
56
57
58
59
60

<u>Author-supplied statements</u>

Relevant information will appear here if provided.

Ethics

Does your article include research that required ethical approval or permits?:
This article does not present research with ethical considerations

Statement (if applicable):
CUST_IF_YES_ETHICS :No data available.

Data

It is a condition of publication that data, code and materials supporting your paper are made publicly available. Does your paper present new data?:
Yes

Statement (if applicable):
The datasets supporting this article are available as part of the supplementary material.

Conflict of interest

I/We declare we have no competing interests

Statement (if applicable):
CUST_STATE_CONFLICT :No data available.

Submitted to Phil. Trans. R. Soc. A - Issue

Page 2 of 34

Author for correspondence:

Sebastian A. Altmeyer

e-mail:

sebastian.andreas.altmeyer@upc.edu

Arrow-shaped elasto-inertial rotating waves

Jose M. Lopez[1], Sebastian A. Altmeyer[1]

[1] Department of Fisica Aplicada, Universitat Politècnica de Catalunya, Girona s/n, Modul B4 Campus Nord, 08034 Barcelona, Spain

We present direct numerical simulations of the Taylor–Couette flow of a dilute polymer solution when only the inner cylinder rotates and the curvature of the system is moderate ($\eta = 0.77$). The finitely extensible nonlinear elastic-Peterlin (FENE-P) closure is used to model the polymer dynamics. The simulations have revealed the existence of a novel elasto-inertial rotating wave characterized by arrow-shaped structures of the polymer stretch field aligned with the streamwise direction. This rotating wave pattern is comprehensively characterized, including an analysis of its dependence on the dimensionless Reynolds and Weissenberg numbers. Other flow states having arrow-shaped structures coexisting with other types of structures have also been identified for the first time in this study and are briefly discussed.

Page 3 of 34

Submitted to Phil. Trans. R. Soc. A - Issue

1. Introduction

In the century that has elapsed since the pioneering work of G. I. Taylor [1], the Taylor–Couette flow (TCF), i.e. the fluid flow contained in the annular gap between two vertical concentric cylinders, has become one of the most prominent models for investigating flow pattern formation, instabilities, and turbulence in rotating shear flows [3–5,12]. This popularity has been partly motivated by the fact that, in many configurations of this system, the transition to the turbulence is supercritical, i.e. it occurs through a well-defined sequence of linear instabilities to flow patterns of increasing spatio-temporal complexity eventually leading to turbulence. The specific characteristics of these flow patterns depend crucially on the geometry of the apparatus (the curvature and the length-to-gap aspect ratio), the container boundaries and the relative rotation of the cylinders. However, it is frequently observed that the transition from axisymmetric to three-dimensional flow gives rise to waves that propagate in the azimuthal direction while keeping a constant shape. These flow states are known as rotating waves and appear when the system undergoes a Hopf bifurcation that breaks its SO(2) symmetry. The best-known example of a rotating wave pattern is the so-called wavy vortex flow, which emerges from the Taylor vortices as the inner cylinder rotation speed increases for a wide range of curvatures and aspect ratios [6–11]. Another well-studied example of rotating waves in pure hydrodynamic TCF is the Ribbons pattern (RB), which emerges when the cylinders counter-rotate [12].

While TCF has traditionally been studied using Newtonian fluids, a growing interest has been shown recently in investigating Non-Newtonian cases, especially when the working fluid is a dilute polymer solution. Due to their viscoelastic properties, long-chain polymers (even in small amounts) may substantially change the stability and spatio-temporal characteristics of the flow with respect to those in the Newtonian case. First observations of such phenomenon date back to about thirty years, with the detection of flow instability in the absence of inertia [18–20]. These studies were followed by a number of experimental works that explored in detail the formation of flow patterns depending on the relative importance between inertial and elastic effects [21,22,26–28]. A wide range of flow patterns was discovered, in many cases coexisting for the same values of the control parameters (the Reynolds and Weissenberg numbers), and it was concluded that observing one or more flow states was highly sensitive to polymer properties, initial conditions, and experimental protocol. One of the most typical states reported in these studies was the RB pattern, a rotating wave formed by two (symmetry degenerated) spiral waves that propagate axially in opposite senses [21,22]. As for Newtonian cases, viscoelastic RB arise from a supercritical Hopf bifurcation of the Circular Couette flow (CCF), but unlike Newtonian fluids, it is not necessary that the cylinders counter-rotate (they are observed even in the classical setup, where only the inner cylinder rotates). Depending on the flow's elasticity, they may occur at rotation speeds one order of magnitude smaller than those at which rotating waves exist in isothermal Newtonian TCF, and they have been found to play a major role in several transition routes to elasto-inertial turbulence (EIT) [17,25]. Other coherent states which are frequently encountered in experiments on TCF of a dilute polymer solution are diwhirls (DW), oscillatory strips (OS), disordered oscillations (DO) or flames (FL) [21,22,26–28]. However, unlike RB, the transition to these flow states, which may occur either from CCF or RB, is abrupt and highly hysteretic.

These coherent states could not be replicated in simulations until the late 2000s [23,24]. The use of the FENE-P (Finite extensibility nonlinear elastic-Peterlin) closure was critical to the success of these simulations because it included important effects of the polymer's finite extensibility that had been previously overlooked in numerical works. In addition to demonstrating the ability of the FENE-P model to accurately simulate polymer dynamics, the authors detailed the spatio-temporal characteristics of the flow states they discovered. However, because the parameter space was not thoroughly explored, there could be many more coherent states than

3

those reported in these studies. Since then, there has been a growing interest in studies aimed at characterizing elasto-inertial turbulence (EIT) [29–31] and no further studies (both numerical and experimental) on flow pattern formation and transition to the EIT have been performed until very recently [13–17,42]. Given the problem's large parameter space, the large number of states that can coexist for the same values of the control parameters, and the scarcity of numerical studies on viscoelastic flow patterns, it is reasonable to expect previously unreported states to emerge in numerical studies on these flows.

Whereas for TCF, coherent elasto-inertial flow patterns have been studied for nearly three decades, for parallel shear flows, only recently the first coherent viscoelastic structure has been found in simulations of a two-dimensional channel flow [32,33]. These structures are travelling waves (the analogue of the rotating waves in parallel flows) that propagate downstream at a speed close to the centreline velocity. The hallmark of these viscoelastic travelling waves is the existence of arrowhead structures in the polymer stretch field which are oriented in the streamwise direction. It has been speculated that these structures may be caused by an increase in the elongational viscosity of the fluid due to polymer stretching in the flow direction [33]. This characteristic suggests that these arrow-shaped structures of polymer stretch may not be exclusive to parallel shear flows, but a universal feature of flow systems where polymers are subjected to elongational flow. In TCF, for instance, polymers are stretched by the primary flow in the azimuthal direction. Hence, an increase in the fluid's elongational viscosity might result in arrow-shaped structures aligned with the azimuthal direction. However, as far as we are aware, no evidence of these structures in flows with curved streamlines has been reported yet.

In this paper, using direct numerical simulations of the TCF of a dilute polymer solution, where the FENE-P closure is used to model the polymer dynamics, we show that arrow-shaped structures of polymer stretch aligned with the streamwise direction (in this case the azimuthal direction) also exist in TCF. These structures are identified in elasto-inertial rotating waves that propagate with a very slow frequency and in chaotic states. We determine the range of existence of the rotating wave solutions in the parameter space defined by the dimensionless Reynolds and Weissenberg numbers and show how the characteristics of the arrow-shaped structures change as these parameters are varied. We also briefly discuss other solution branches found in our study.

2. Problem formulation and methodology

(a) Governing equations and dimensionless parameters

We consider the flow of a dilute polymer solution driven in the annular gap between two vertical, rigid, and independently rotating cylinders of height h. The inner cylinder of radius r_i rotates at angular speed Ω_i and the outer cylinder of radius r_o is kept at rest, i.e. $\Omega_o = 0$. The fluid is incompressible and the dynamics is governed by the Navier-Stokes and continuity equations. An additional equation is needed to describe the temporal evolution of a polymer conformation tensor, $\mathbf{C}$, which contains the ensemble average elongation and orientation of all polymer molecules in the flow. Each polymer molecule is modeled by a finitely extensible elastic dumbbell [38]. The dimensionless equations read

$$\nabla \cdot \mathbf{v} = 0,$$
$$\partial_t \mathbf{v} + \mathbf{v} \cdot \nabla \mathbf{v} = -\nabla P + \frac{\beta}{Re} \nabla^2 \mathbf{v} + \frac{(1-\beta)}{Re} \nabla \cdot \mathbf{T},$$
$$\partial_t \mathbf{C} + \mathbf{v} \cdot \nabla \mathbf{C} = \mathbf{C} \nabla \mathbf{v} + (\nabla \mathbf{v})^T \mathbf{C} - \mathbf{T},$$

(2.1)

where $\mathbf{v} = (u, v, w)$ is the velocity vector field in cylindrical coordinates (r, θ, z), P is the pressure, $\beta = \nu_s/\nu$ indicates the relative importance between the solvent viscosity, ν_s, and the viscosity of the solution at zero shear rate, ν. The length scale of the system is normalized with the gap width,

4

$d = r_o - r_i$, the velocity with the inner cylinder velocity, $\Omega_i r_i$, the pressure with the dynamic pressure, $\rho(\Omega_i r_i)^2$, where ρ is the fluid's density, and the polymer conformation tensor with $k_B T_e / H$, where k_B denotes the Boltzmann constant, T_e is the absolute temperature and H is the spring constant.

The coupling between the polymers and the Navier-Stokes equations is realized through the polymer stress tensor $\mathbf{T}$, which is calculated using the FENE-P model [38],

$$\mathbf{T} = \frac{1}{Wi} \left(\frac{\mathbf{C}}{1 - \frac{tr(\mathbf{C})}{L^2}} - \mathbf{I} \right), \tag{2.2}$$

where $\mathbf{I}$ is the unit tensor, $tr(\mathbf{C})$ is the trace of the polymer conformation tensor, L denotes the maximum polymer extension parameter and Wi is the Weissenberg number (defined below).

Periodic boundary conditions are imposed in the z and θ directions, whereas the boundary conditions at the cylinders are

$$\mathbf{v}(r_i, \theta, z) = (0, 1, 0), \quad \mathbf{v}(r_o, \theta, z) = (0, 0, 0). \tag{2.3}$$

The system is governed by the following independent non-dimensional parameters:

$$
\begin{aligned}
&\text{Reynolds number:} && Re = \Omega_i r_i d / \nu, \\
&\text{Weissenberg number:} && Wi = \lambda / [d / (\Omega_i r_i)] \\
&\text{Radius ratio:} && \eta = r_i / r_o, \\
&\text{Aspect ratio:} && \Gamma = h / d,
\end{aligned}
\tag{2.4}
$$

where λ is the polymer relaxation time and $d/(\Omega_i r_i)$ is the advective time scale.

In this paper, the radius ratio and aspect ratio are fixed to $\eta = 0.77$ and $\Gamma = 2\pi$, respectively. A constant polymer concentration $\beta = 0.871$ is used and the maximum polymer extension parameter L is set to 100, in accordance with recent studies of elasto-inertial turbulence on viscoelastic TCF [16,39–41]. The flow's elasticity level, quantified by the elasticity number $El = Re/Wi$, ranges from 0.01 to 1. The parameter space is explored by either fixing Re and varying Wi or vice versa, and consequently, the value of El changes among simulations. This protocol differs from that in [23,24], the only numerical study on flow pattern formation in viscoelastic TCF conducted to date, where the simulations were performed at a constant El for five different El values ($El = 0.33$, $El = 0.50$, $El = 0.75$, $El = 1$ and $El = 30$). Another difference with respect to this study is the polymer concentration. The polymer solution used in our simulations is nearly 10% more diluted than that used in [23,24] ($\beta = 0.8$ in these references).

(b) Numerical methods

The governing equations (2.1) are solved with the open source code nsCouette [43]. The code is a combination of high-order central finite differences on a Gauss-Lobatto-Chebyshev grid in r and Fourier-Galerkin expansions in z and θ. Decoupling between pressure and velocity field is realized by a Pressure Poisson Equation formulation. The free divergence condition is enforced by using an influence matrix technique, so that this condition is satisfied up to machine error. A second-order accurate predictor-corrector scheme based on the Crank-Nicolson method is used to carry out the time integration (see references [44,45] for further details about the timestepper). Following the customary approach in numerical simulations of viscoelastic flows using pseudo-spectral codes, a small amount of artificial diffusion is added to stabilize the integration. The reason to include this diffusion is the hyperbolic nature of the time evolution equation for $\mathbf{C}$. In the absence of diffusion, integration of this equation often results in an accumulation of numerical error, which in many cases produce numerical breakdown. This issue can be overcome by adding a Laplacian term, $\frac{1}{ReS_c}\nabla^2 \mathbf{C}$, to the right-hand side of this hyperbolic equation, where the Schmidt number, $S_c = \nu/\kappa$, quantifies the ratio between the viscous and artificial diffusivities. In the simulations presented here, S_c has been varied between 50 and 100, so that the artificial diffusion

Submitted to Phil. Trans. R. Soc. A - Issue

Page 6 of 34

coefficient, $\frac{1}{ReSc_c}$, is of the order of 10^{-4}. Several tests using larger Sc values (Sc up to 200 were tested) have been conducted to verify that further reduction in the diffusion coefficient does not alter significantly the results of the simulations. The number of radial nodes and Fourier modes used in the computations were $m_r = 64$, $m_\theta = 33$ and $m_z = 256$, whereas the time step size was set to 5×10^{-3}.

3. Arrow shaped structures of polymer stretch

To probe whether arrow-shaped structures of polymer stretch exist in viscoelastic TCF, we have conducted simulations at low Re values ($Re \leq 100$) while keeping $Wi = 15$. The elasticity number, $El = Wi/Re$, in these simulations falls within the range $0.15 \leq El \leq 0.75$, which is consistent with the elasticity levels at which arrowhead structures have been observed in channels. The simulations were started from the laminar state, previously computed, which was perturbed by a disturbance of the form,

$$u = A(r - r_i)(r - r_o)cos(\theta + kz) \tag{3.1}$$

$$w = -A\frac{(r - r_i)(r - r_o)}{r}(5r^2 - 3(r_i + r_o)r + r_i r_o)\frac{sin(\theta + kz)}{k}, \tag{3.2}$$

where k is the axial wavenumber and A denotes the amplitude of the perturbation. If the value of A is sufficiently large, the simulations converge to a rotating wave with azimuthal wavenumber m=1. The amplitude threshold required to cause the instability is small (it can be as small as $A \sim O(10^{-8})$ at the largest Re investigated), yet below this threshold the energy of the perturbation decays and the laminar state persists. This indicates that these rotating wave patterns are driven by nonlinear effects. We note that the existence of subcritical instabilities triggered by very low amplitude thresholds is consistent with recent findings in other studies on viscoelastic flows at low Reynolds numbers [47,48]. Depending on the value of k used in the initial condition, flow patterns with three or four pairs of counter-rotating vortices were obtained. In the following, we will restrict the discussion to the case where the flow pattern has four vortex pairs.

The upper panels of figure 1 show colour maps of the trace of the polymer conformation tensor, $tr(\mathbf{C})$, normalized with the maximum elongation of the polymers, L^2, in a cylindrical section (θ,z) at three different radial locations (indicated on top of each panel) for a simulation conducted at Re= 90. This quantity indicates the degree of stretching of the polymer chains. High values of $tr(\mathbf{C})/L^2$ (dark regions) denote highly stretched polymers, whereas low values of $tr(\mathbf{C})/L^2$ (lighter regions) indicate that polymers are weakly stretched. As is evident from the figure, the most distinctive feature of this flow state is the existence of regions of highly stretched polymers in the shape of an arrow. Due to this characteristic, it will be hereafter referred to as arrow-shaped rotating wave (ArrowRW). These arrow-shaped structures are observed across the radial gap, except for the regions very close to the cylinders, but their shapes differ depending on the radial location. As one moves from the outer to the inner cylinder (from right to left in the figure), the body of the arrow progressively shortens, and the axial extent of the arrowhead increases.

To illustrate the correspondence between polymer stretch and flow velocity, the lower panels of the figure 1 show colour maps of the radial velocity in the same section and at the same time instant as the upper panels. Positive velocity (red areas) denotes fluid motion from the inner to the outer cylinder, i.e outflows, whereas negative velocity (blue areas) indicates fluid moving from the outer to the inner cylinder, i.e. inflows. When the upper and lower rows of the figure are compared, it becomes evident that the arrow-shaped structures of highly stretched polymers are associated with inflow regions, whereas outflows occur in areas where the polymer stretch is lower (less than 25% of L^2). The wake of the arrows, on the other hand, corresponds to the vicinity of the boundaries between inflows and outflows, where the radial velocity is close to zero. As seen, the velocity in the inflows is higher than that of the outflows. This characteristic is caused by the elastic force created by the stretched polymers. This force acts radially inward
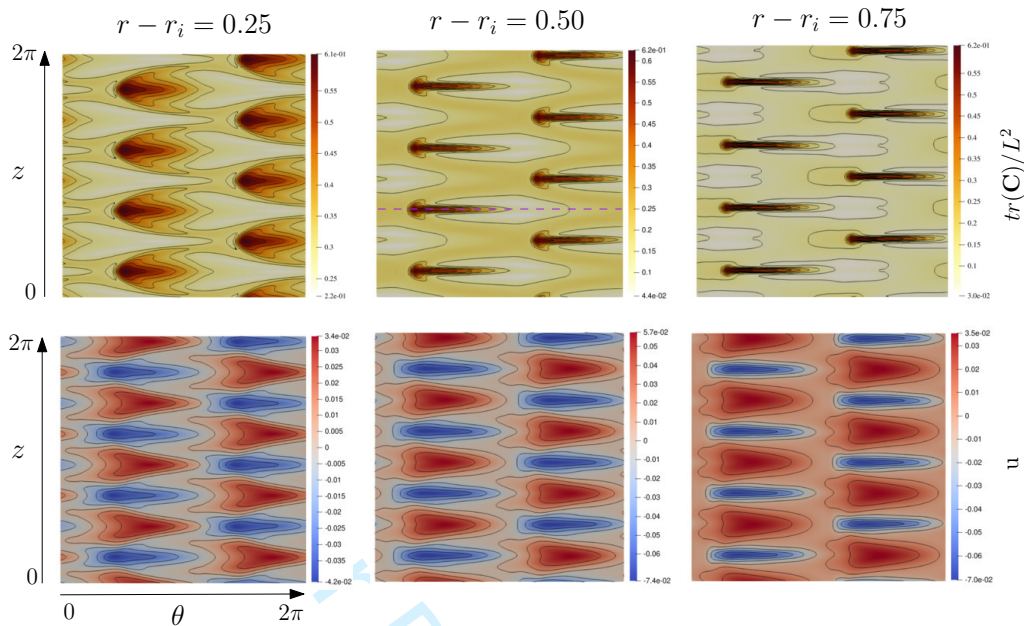
Page 7 of 34

Submitted to Phil. Trans. R. Soc. A - Issue

Figure 1. (Color online) The upper panels show colour maps of the trace of the polymer conformation tensor, $tr(\mathbf{C})$, normalized with the maximum polymer extension, L^2, in cylindrical sections (θ, z) at three different radial locations. Dark (light) regions indicate regions where polymers are highly (slightly) stretched. The lower panels display colour maps of the radial velocity, u, at the same time instant and in the same cylindrical sections as the upper panels. Red (blue) areas indicate outflows (inflows). The example shown corresponds to a snapshot of a simulation with $Re = 90$, $L = 100$, $\beta = 0.871$, and $Wi = 15$. Eight contours evenly spaced across the entire range of values (indicated in the colorbar) are shown in each case. The flow direction is from left to right.

and hence enhances fluid motion through the inflows while slowing down the motion through the outflows. This creates an asymmetry between inflows and outflows (the axial extent of the outflows is larger than that of the inflows) which has been discussed in detail in [46] and [16]. The highest degree of asymmetry occurs near the outer cylinder, where the elastic force exhibits strong localized peaks that result in strong localized inflow jets (note that the axial extent of the outflow regions here is more than twice that of the inflow regions, see panel corresponding to $r - r_i = 0.75$). However, as we move towards the inner cylinder, the magnitude of the elastic force decays gradually, and consequently, the degree of asymmetry between inflows and outflows also diminishes (see panels for $r - r_i = 0.50$ and $r - r_i = 0.25$). The changes observed in the arrow-shaped structures when these are plotted at distinct radial locations (upper panels) can thus be ascribed to the radial dependence of the elastic force and how this modifies the axial extent of the inward motion.

To provide a simpler quantitative characterization of the polymer stretch, we show in figure 2 the variation of $tr(\mathbf{C})/L^2$ along the azimuthal direction at fixed radial (mid-gap) and axial ($z = 2.25$) locations for the same snapshot shown in figure 1 (i.e. along the purple dashed line shown in that figure). We note that the same plot is obtained if $tr(\mathbf{C})/L^2$ is plotted as a function time at a fixed azimuthal location (time is shown in the upper abscissa of the figure). This happens because in rotating waves the variation in θ is commensurate with the temporal evolution of the flow pattern. Figure 2 shows that the emergence of the arrow-shaped structures is associated with an abrupt local increase of $tr(\mathbf{C})/L^2$. The maximum value of $tr(\mathbf{C})/L^2$ is achieved in the head of the arrow, shortly after the sudden increase takes place, and it can be as large as 0.75 (i.e. 75% of the maximum polymer elongation) for the largest values of Re and Wi simulated in this study.
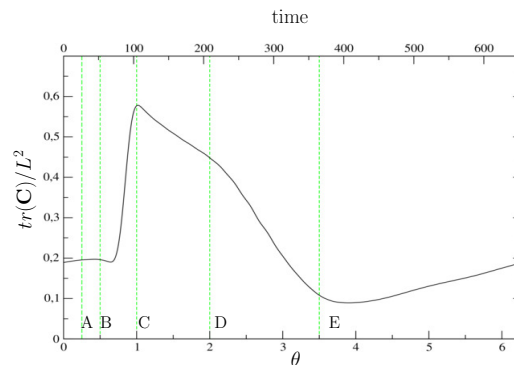
Figure 2. Trace of the polymer conformation tensor, normalized by L^2, obtained at the mid-gap ($r - r_i = 0.5$)and $z/d = 2.25$ as a function of θ (lower abscissa) and time (upper abscissa). The values of θ for which meridional sections are shown in figure 3 are represented as green dashed lines.

The decay of $tr(\mathbf{C})/L^2$ exhibits two phases: a slow decay that coincides with the body of the arrow and a sharper decay that occurs in the wake behind the arrow ($2 < \theta < 3.5$). The minimum value of $tr(\mathbf{C})/L^2$ is reached in the latter region and it is in all simulations lower than 10% of the maximum polymer elongation. After the minimum, $tr(\mathbf{C})/L^2$ increases gradually until it reaches a value of nearly 0.2 which remains constant before the emergence of the arrow-shaped structure.

We finally show in figure 3 the radial dependence of the polymer stretch (upper row) and flow streamlines (lower row) as a function of θ. The values of θ at which snapshots are displayed are shown as dashed lines in figure 2. The leftmost panels (A, $\theta = 0.25$) illustrate the flow upstream of the arrow-shaped structure, far from the arrowhead. Polymers here are more stretched in the region near the inner cylinder. This circumstance appears to be related to the emergence of flow recirculation zones near the inner cylinder (see the leftmost panel of the lower row), which displace the main vortices towards the outer cylinder. As the arrowhead is approached, the intensity of the vortices increases and the recirculating vortices near the inner cylinder weaken. As a result, polymers get increasingly more stretched near the outer cylinder (see panels B, for $\theta = 0.5$). Jets of highly stretched polymers emanate then from the outer cylinder and move towards the inner cylinder through the inflows (see panels C, which corresponds to the arrowhead, $\theta = 1$). Vigorous counter-rotating vortex pairs, with a clear asymmetry between inflows and outflows, as described above, extend across the entire radial gap (lower C panel). This situation continues as one moves toward the bottom end of the arrow-shaped structure. When the jet of highly stretched polymers meets the inner cylinder, it begins to spread along the wall (see panel D, for $\theta = 2$), and polymers get progressively more stretched in this region. The initial situation where the recirculations zones appear near the inner cylinder and the vortices move towards the outer cylinder is eventually recovered (see panel E, for $\theta = 3.5$) and the cycle starts again (with the vortices and regions of highly stretched polymers shifted by half a wavelength with respect to the first half of the rotation period).

4. *Re* and *Wi* parameter dependence

To establish the range of existence of the ArrowRW solution in the *Wi-Re* parameter space and how the characteristics of the arrow-shaped structures change with varying these parameters, we have conducted natural continuation of this flow state. The black line in figure 4 (a) shows the deviation of the volume averaged kinetic energy, k_e, with respect to its laminar value, for the ArrowRW state at the *Re* values at which this solution is found when *Wi*$= 15$. We note that
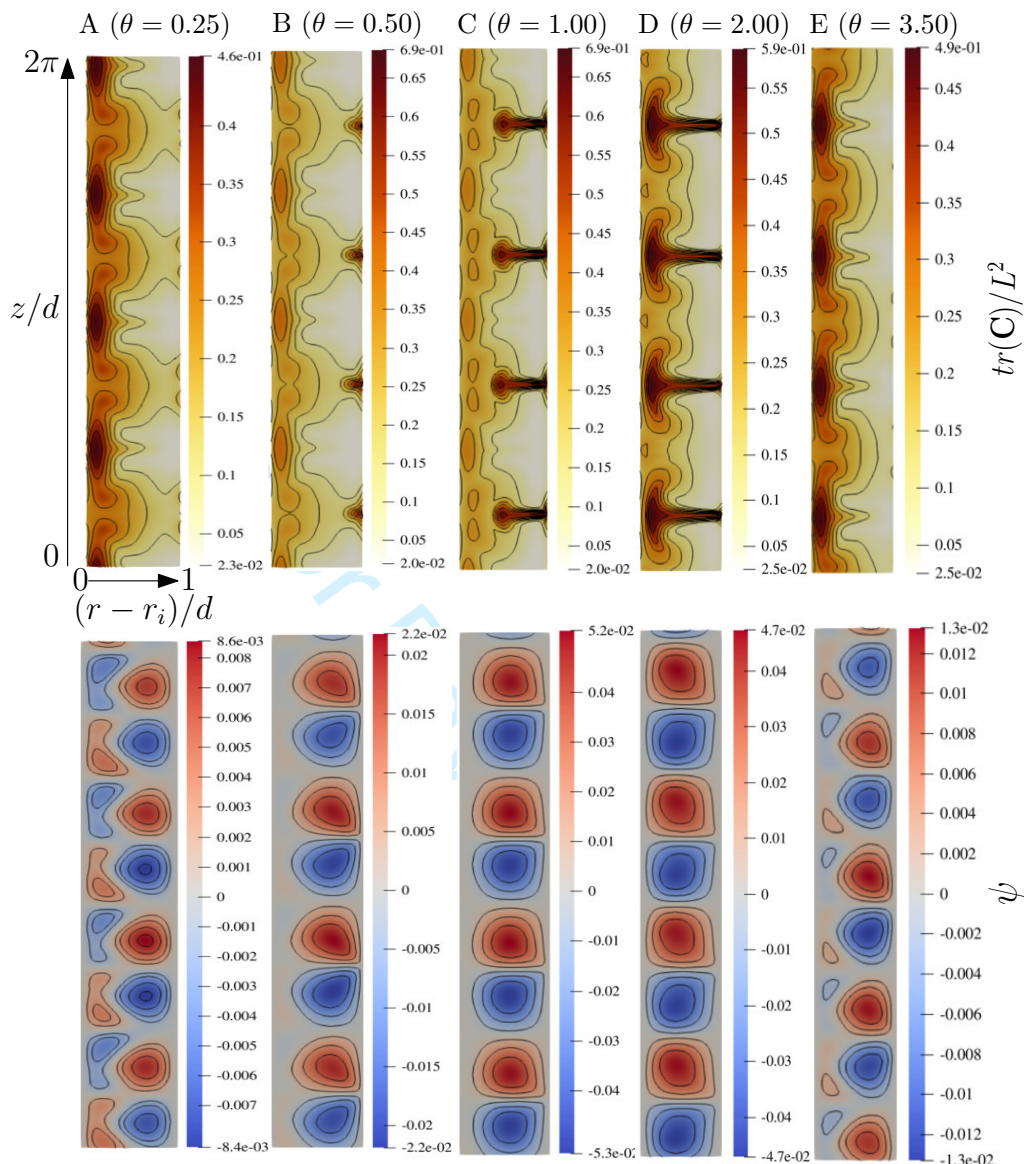
Page 9 of 34

Submitted to Phil. Trans. R. Soc. A - Issue

Figure 3. (Color online) Colour maps of polymer stretch (upper row) and flow streamlines ψ (lower row) shown in meridional sections (r, z) obtained at the values of θ indicated at the top of each panel (and shown as dashed (green) lines in the figure 1). Eight contours evenly spaced across the full range of values have been added to each panel.

for this *Wi* value, the base flow is linearly stable. The ArrowRW solution vanishes at a saddle-node bifurcation that takes place at $Re \approx 20$. It should be noted that this value of Re is well below that at which Taylor vortices appear in the Newtonian case ($Re \approx 90$), clearly showing that the instability relies on the interplay between inertia and elasticity. The lower branch solution that continues at lower energy towards larger Re values is unstable, but it could be detected by using the bisection method introduced by [49] (see black dashed line in figure 4 (a)). Only a few points of this solution branch have been computed, as flow states here are characterized by very weakly stretched polymers and arrow-shaped structures are no longer observed. To follow the ArrowRW solution branch near the saddle-node, it is necessary to vary Re in very small steps. If the change in Re is too large, the simulations converge to a different flow state, labeled LArrowRW in the

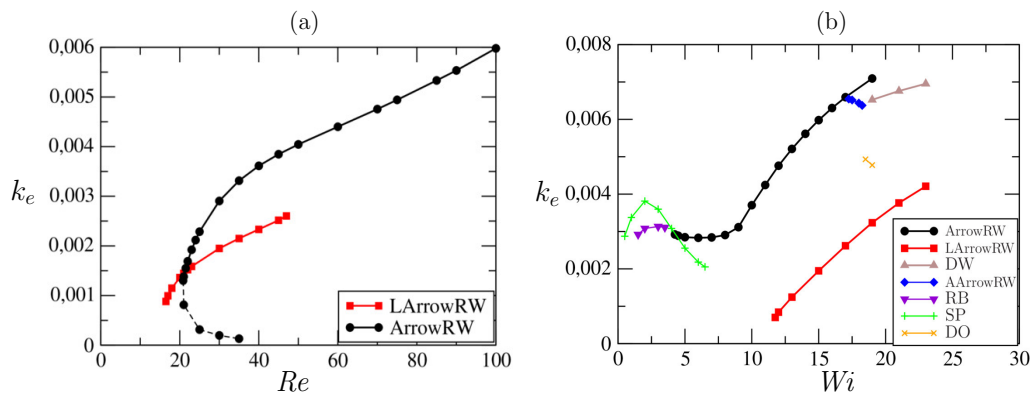Submitted to Phil. Trans. R. Soc. A - Issue

Page 10 of 34

Figure 4. (Color online) Variation of the deviation of the volume average kinetic energy in the flow states found in the present study as the *Re* and *Wi* numbers are varied. Note that the volume average kinetic energy corresponding to the laminar state has been subtracted. (a) *Re* number dependence when *Wi*= 15 and (b) *Wi* number dependence when *Re*= 100, except for the LArrowRW state where *Re*= 30. The acronyms shown in the legend stand for: arrow shaped rotating wave (ArrowRW), localized arrow-shaped rotating wave (LArrowRW), asymmetric arrow-shaped rotating wave (AArrowRW), spirals (SP), diwhirls (DW), ribbons (RB) and disordered oscillations (DO).

figure, which is characterized by azimuthally localized arrow-shaped structures (This state is illustrated in figure 7 (c) and described in more detail in section 5). The LArrowRW coexists with the ArrowRW for $20 \lessapprox Re \lessapprox 45$, and it could be followed up to $Re \approx 16.5$, a value slightly lower than that at which the ArrowRW disappears. Below this threshold, the flow laminarises.

The highest *Re* value at which the ArrowRW exists for *Wi*= 15 is *Re*= 100. With further increase in *Re*, the flow pattern begins to exhibit additional modulations and complex spatio temporal dynamics set in. These states are, however, outside the scope of this paper and will be discussed elsewhere. As expected, polymer stretch increases with increasing *Re* due to the increase in the magnitude of the mean azimuthal velocity, reaching a maximum value of 75% of L^2 for *Re*= 100. The upper row of the figure 5 shows colour maps of the polymer stretch in a cylindrical section at the mid-gap for the simulations performed at *Re*= 25 and *Re*= 50. Along with the middle panel in the upper row of figure 1, for *Re*= 90, these figures illustrate the variation of the structures of polymer stretch as the *Re* number increases along the upper branch solution while holding the *Wi* number constant. For *Re* values near the saddle-node bifurcation (see panel for *Re*= 25), the arrow-shaped structures are not yet evident. The maximum polymer stretch here is still rather moderate (less than 50% of the maximum polymer extension) and this results in oval-shaped structures, where the azimuthal extent is only slightly larger than the axial extent (see darker zones). As *Re* increases and the stretching of the polymers increases, the structures become increasingly more elongated in the azimuthal direction and the arrow shape emerges. The right upper panel of the figure 5 shows that for *Re*= 50, the arrow-shaped structures can be already clearly distinguished, even though the highest polymer stretch is still not too large (only slightly above half of L^2).

The black line in figure 4 (b) illustrates the variation of the ArrowRW state when *Re*= 100 and *Wi* is varied. The minimum *Wi* number at which the solution could be followed is *Wi*= 4.25. Below this threshold, the ArrowRW becomes unstable and simulations converge to either RB or Spirals (SP). Two distinct trends are observed in the energy of the ArrowRW. It remains nearly constant when $4.25 \leq Wi \leq 9$ and increases with increasing *Wi* when *Wi*> 9. Despite the transition between the two regimes appearing to be rather smooth, the flow structures are qualitatively and quantitatively very different. Whereas for large *Wi* numbers, the arrow-shaped structures of highly stretched polymers shown in the figure 1 are observed, in the regime where the energy
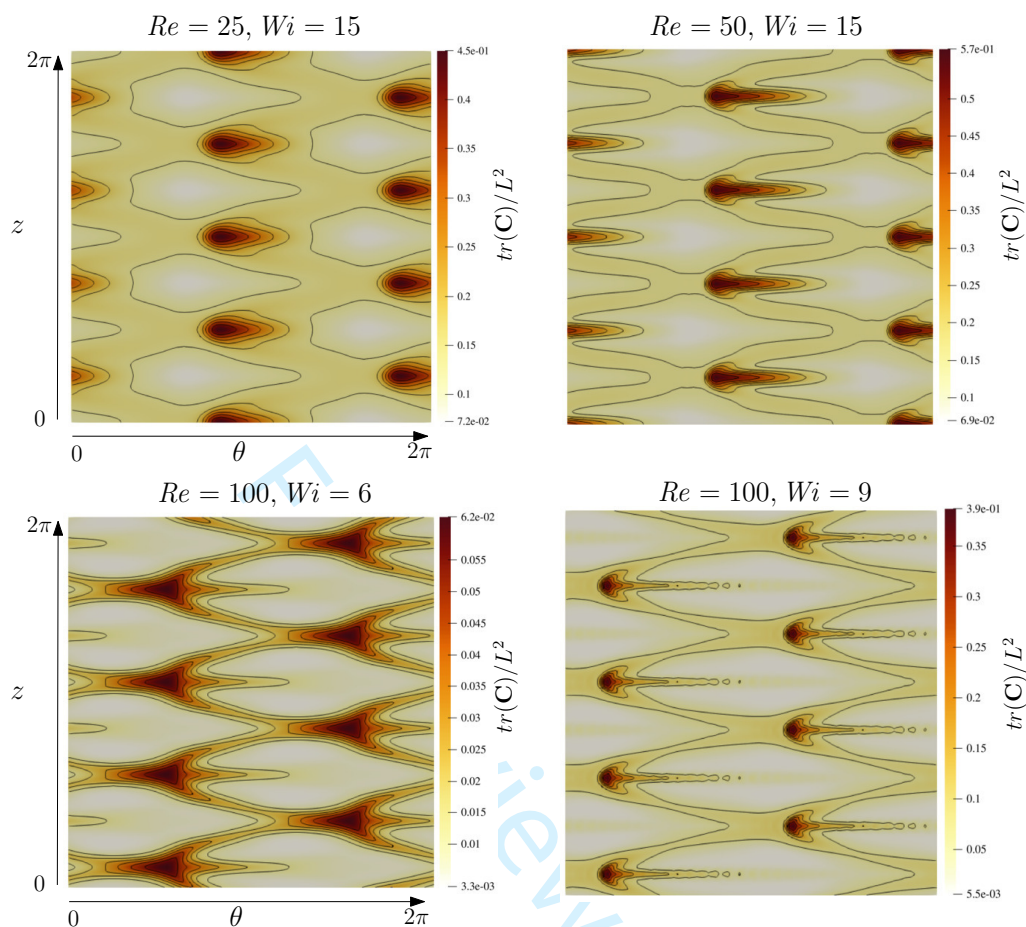
9

10

Figure 5. (Color online) Variation of the structures of polymer stretch as the *Re* (upper row) and *Wi* (lower) numbers are varied. Cylindrical sections (θ,z) obtained at the mid-gap are shown. Eight contours evenly spaced across the full range of values have been added to each panel.

is almost constant, the structures of polymer stretch take the form of a fork oriented in the flow direction (see left panel of figure 5 for *Wi*= 6). Interestingly, the amount of polymer stretch in these structures is surprisingly low (below 10% of L^2). It must be noted that the simulation for *Wi*= 4.25 was run for nearly 10000 advective time units. The solution persisted for this time and there was not any sign that there could be a change in the flow pattern with further simulation time. Hence, this surprising solution appears to be stable. As *Wi* increases, the forked-shaped structures are gradually replaced by arrow-shaped structures. The lower right panel shows the structures for the simulation conducted at *Wi*= 9, which marks the transition between the regimes of constant and increasing energy. As seen, arrow-shaped structures of moderately stretched polymers can already be identified at this *Wi* value. The largest *Wi* at which the ArrowRW state was found is *Wi*= 19. Above this value, the solution becomes unstable and the simulations converge to a stationary pattern of elastically induced vortices known as diwhirls (DW, brown line in figure 4 (b)). The dynamics of the DW have been recently shown in detail in [16] and thus will not be discussed here. Other solution branches, labeled as AArrowRW and DO in the figure, were also found at large *Wi* numbers and will be discussed in section 5.

All the arrow-shaped rotating waves found in this study propagate very slowly, with a rotation frequency (calculated from fast Fourier transform of a time series of the radial velocity) of the
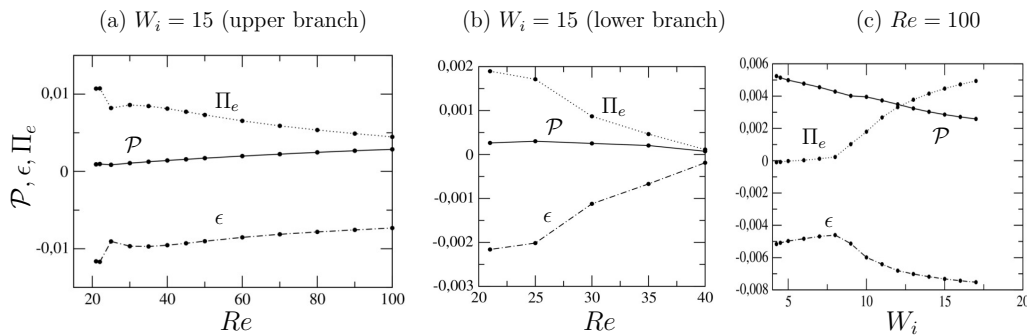
Submitted to Phil. Trans. R. Soc. A - Issue

Page 12 of 34

Figure 6. Variation of the inertial ($\mathcal{P}$), viscous (ϵ) and polymeric (Π_e) contributions to the integral energy balance (i.e. kinetic energy budgets) in (a) upper branch solution of the ArrowRW for $W_i = 15$, (b) lower branch solution of the ArrowRW for $W_i = 15$ and (c) ArrowRw for $Re = 100$ and varying W_i. In each panel, $\mathcal{P}$, ϵ and Π_e are shown as solid, dash-dotted and dotted lines, respectively.

order of $f \sim 10^{-3}(\Omega_i r_i)/d$. Moreover, it is observed that the rotation frequency decreases as *Re* or *Wi* increases.

We finally investigate the relationship between the changes observed in the volume averaged kinetic energy as *Re* and *Wi* are varied and the physical mechanisms governing the physics of this problem (i.e. inertial, viscous, and elastic effects). To that extent, we have calculated the inertial ($\mathcal{P}$), viscous (ϵ), and polymeric (Π_e) contributions to the integral energy balance of the ArrowRW solution. For viscoelastic flows, the integral energy balance reads [50],

$$\int_V \mathcal{P} dV - \int_V \epsilon dV - \int_V \Pi_e dV = 0, \tag{4.1}$$

and $\mathcal{P}$, ϵ and Π_e are calculated as,

$$\mathcal{P} = -\overline{u'v'}\frac{\partial \overline{v}}{\partial r} + \overline{u'v'}\frac{\overline{v}}{r}, \tag{4.2}$$

$$\epsilon = \frac{2\beta}{Re}\overline{S':S'}, \tag{4.3}$$

$$\Pi_e = \frac{1-\beta}{Re}\overline{S':T'}. \tag{4.4}$$

Here, the overline denotes mean quantities, $S' = (\nabla \mathbf{v}' + \nabla \mathbf{v}'^T)/2$ indicates the rate of strain tensor and the prime symbol denotes deviations of the velocity or polymer stress tensor from their mean values. It must be noted that $\mathcal{P}$ and ϵ always act as a source and a sink of energy, respectively. However, Π_e can be either a source or a sink depending on whether the sign of the integral is negative or positive (note that there is a minus sign in front of the integral). In panel (a) of figure 6, it is shown how the values of these three integrals (including the sign in front of them) vary with *Re* along the upper branch solution curve. As seen, for all *Re* numbers, the polymeric contribution is the dominant energy source (polymers are injecting energy into the flow), reflecting again the elastic nature of the ArrowRW solution. At the lowest values of *Re* (near the turning point), the contribution of Π_e is larger than that of $\mathcal{P}$ by two orders of magnitude. However, as *Re* increases, the contribution of $\mathcal{P}$ increases, and the contribution of Π_e decreases, so that at the largest *Re* values where the ArrowRW solution exists, they are similar in magnitude. This behaviour was expected, as in this analysis we keep $W_i = 15$, and so, as *Re* increases, the relative importance of inertial effects against elastic effects increases. In panel (b), the variation of the contributions of $\mathcal{P}$, ϵ, and Π_e is shown for the lower branch solution curve when $W_i = 15$. While the contribution of Π_e continues to be the dominant energy source near the turning point, its magnitude decays fast as *Re* increases and it becomes of the same order of magnitude as the inertial contribution at $Re \approx 30$. These analyses show that, at this *Wi* value,

Page 13 of 34

Submitted to Phil. Trans. R. Soc. A - Issue

steady ArrowRW states appear only when the flow is entirely dominated by elasticity, and that these solutions become unstable as the inertial effects become comparable to elastic effects. Finally, panel (c) of 6 illustrates the same analysis for the case in which $Re = 100$ and W_i is varied. It is observed that, at low Wi numbers, inertia is the dominant energy source. Although the net polymeric contribution at these Wi is positive and hence polymers also act as an energy source, its magnitude is very small when compared to the inertial contribution. Interestingly, this low contribution of the polymers to the integral energy balance persists until $Wi \approx 9$ is achieved, and it is thus consistent with the regime where the volume averaged kinetic energy is constant and stable forked-like structures are observed. Beyond this threshold, the contribution of Π_e grows quickly with increasing Wi, and this, along with the gradual decrease in the inertial contribution, results in a flow regime similar to that described in panel (a), where the polymeric contribution is the main energy source. It is when this happens that arrow-shaped structures of highly stretched polymers are observed.

5. Other solution branches

Having presented the ArrowRW solution in detail, we next focus on other solution branches where arrow-shaped structures of polymer stretch are also present. The first of these solutions, which has been dubbed asymmetric arrow rotating wave (AArrowRW), emerges at $Wi \approx 17.3$ (for $Re = 100$) when the ArrowRW undergoes a symmetry-breaking bifurcation that breaks the axial symmetry of the structures. This characteristic becomes clear when figure 7 (a), which illustrates the AArrowRW state at $Re = 100$ and $Wi = 18$, is compared with figure 1 (middle panels). Whereas for the ArrowRW, the arrow-shaped structures (including the wake) are symmetric with respect to the horizontal plane passing through the axis of the arrow, this symmetry is not preserved by the AArrowRW. In this latter state, there is an increase of the polymer stretch in the lower half of the structures (see that the colour intensity in this region right after the arrowhead is slightly darker than in the upper half), which results in the wake extending over a larger azimuthal distance than in the upper half. This asymmetry is, of course, also reflected in the structures of the radial velocity. By comparing the left and right panels in figure 7 (a), it can be seen that the increase in polymer stretch taking place in the lower half of the arrows is associated with shear layers that form in the boundaries between inflows and outflows. These shear layers are readily identified in the figure as regions where the contours of radial velocity are closely spaced, thereby indicating strong velocity gradients.

The AArrowRW is stable in a narrow range of Wi numbers, $17.3 \lesssim Wi \lesssim 18.4$ for $Re = 100$ (see blue diamonds in figure 4 (b)). Within this range, the symmetrically related state, AArrowRW$^* = K_z$AArrowRW, has also been found (not shown). It has the same characteristics as the AArrowRW state, but shear layers and higher polymer stretch are in this case observed in the upper half of the arrow-shaped structures. It should also be noted that, unlike the ArrowRW state, the kinetic energy of the AArrowRW decreases monotonically as Wi increases. Following the solution beyond $Wi \gtrsim 18.4$, the flow becomes chaotic and the kinetic energy decreases markedly (see states denoted by (orange) cross marks in figure 4 (b)). Irregular arrow-shaped structures are transiently observed in the polymer stretch field, coexisting with strips of highly stretched polymers that extend over the entire azimuthal length (see figure 7 (b)). Unlike the flow states described above, arrow-shaped structures appear at random θ and z locations and their azimuthal extent is highly variable. Due to this randomness, the property that the structures are shifted by half a wavelength every half a rotation period is evidently absent. This chaotic flow is consistent with a state of disordered oscillations (DO), which is the term used in viscoelastic Taylor–Couette flow to denote chaotic flow patterns characterized by large-scale irregular flow structures [21,23–25,39]. This is, however, the first time that a DO state with arrow-shaped structures is reported.

Another flow state where arrow-shaped structures also appear is found at low Re values, near the saddle-node bifurcation point of the ArrowRW (see (red) squares in 4 (a)). Such state, which

is presented in figure 7 (c) for $Re = 30$ and $Wi = 15$, exhibits axially symmetric arrow-shaped structures of polymer stretch which are similar in length and magnitude to those of the ArrowRW. However, they appear only in one half of the system, i.e. over half a rotation period. We have dubbed this flow state as localised arrow shaped rotating wave (LArrowRW). We would like to note that localisation of structures in TCF usually happens in the axial direction or in both axial and azimuthal directions, resulting in patches. The azimuthal localisation observed in this viscoelastic flow state is thus quite unusual and the mechanism behind it is still not understood. The parameter range in which the LArrowRW state exists is smaller than that for the ArrowRW state, for both Re and Wi numbers (see (red) squares in figure 4). When $Wi = 15$, the minimum Re value up to which the LArrowRW can be followed is $Re \approx 16.5$, where the flow recovers its laminarity, whereas the highest Re value at which this state exists is $Re \approx 45$. Beyond this value, this solution branch becomes unstable and the simulations converge to the ArrowRW state. When the flow pattern is continued in Wi, while keeping $Re = 30$, the flow laminarises below $Wi \approx 11.5$. The kinetic energy of the LArrowRW increases monotonically with increasing Wi (states with nearly constant energy have not been found for this solution) until at $Wi \approx 23$, this solution loses stability to the ArrowRW.

Flow structures which do not exhibit arrow-shaped structures have also been found at low Wi numbers. These are well-known structures of TCF, the so-called spirals (SP) and ribbons (RB) states [3,12]. SP are found to exist when $0.5 \lessgtr Wi \lessgtr 6.5$, whereas RB exist in a narrower region, $1.5 \lesssim Wi \lesssim 3.5$ (see figure 4 (b)). These flow patterns have been widely analysed in the literature and will not be further discussed here.

6. Conclusion

Using direct numerical simulations of the governing equations, we have demonstrated the existence of axially localized, arrow-shaped structures of polymer stretch in the TCF of a dilute polymer solution. These structures have been identified in both rotating waves and in disordered flow patterns. An analysis of the integral energy balance has revealed that stable arrow-shaped rotating waves occur when the energy input associated with elastic mechanisms is the leading order term. In contrast, when the elastic and inertial contributions are comparable, these solutions become unstable.

Recently, arrow-shaped regions of highly stretched polymers have also been identified in viscoelastic channel flow at elasticity levels similar to those investigated here. Despite these structures being qualitatively distinct from those we report, it is interesting to note that in both cases they are aligned with the mean flow direction (the azimuthal direction in TCF and the axial direction in channels). This observation appears to support the hypothesis in [33] that arrow-shaped structures are caused by an increase in the elongational viscosity of the flow due to polymer stretching in the primary flow direction, and it suggests that they could exist in any viscoelastic fluid flow where there is a dominant velocity component.

Among the rotating waves found in the study, it is particularly interesting the LArrowRW state, where the arrow-shaped structures are only found in half of the system. Further research is needed to understand the mechanism behind this surprising feature. It also remains to see if these rotating waves persist in a real TCF system, where the assumption of axial periodicity adopted in our study is not fulfilled. Simulations with axial boundary conditions mimicking the experimental end-plates and/or laboratory experiments will be needed to answer this question. It should be noted that although the polymer stretch field cannot be easily measured in experiments, we have shown that another distinctive feature of these rotating waves is that the radial velocity structures are also arrow headed and point in the flow direction. Since the temporal evolution of the rotating wave pattern is equivalent to its azimuthal dependence, a space time plot of the radial velocity obtained at the mid-gap and at constant θ, over a rotation period, would be identical to

13

Page 15 of 34

Submitted to Phil. Trans. R. Soc. A - Issue

(a) $Re = 100$, $Wi = 18$

(b) $Re = 100$, $Wi = 20$
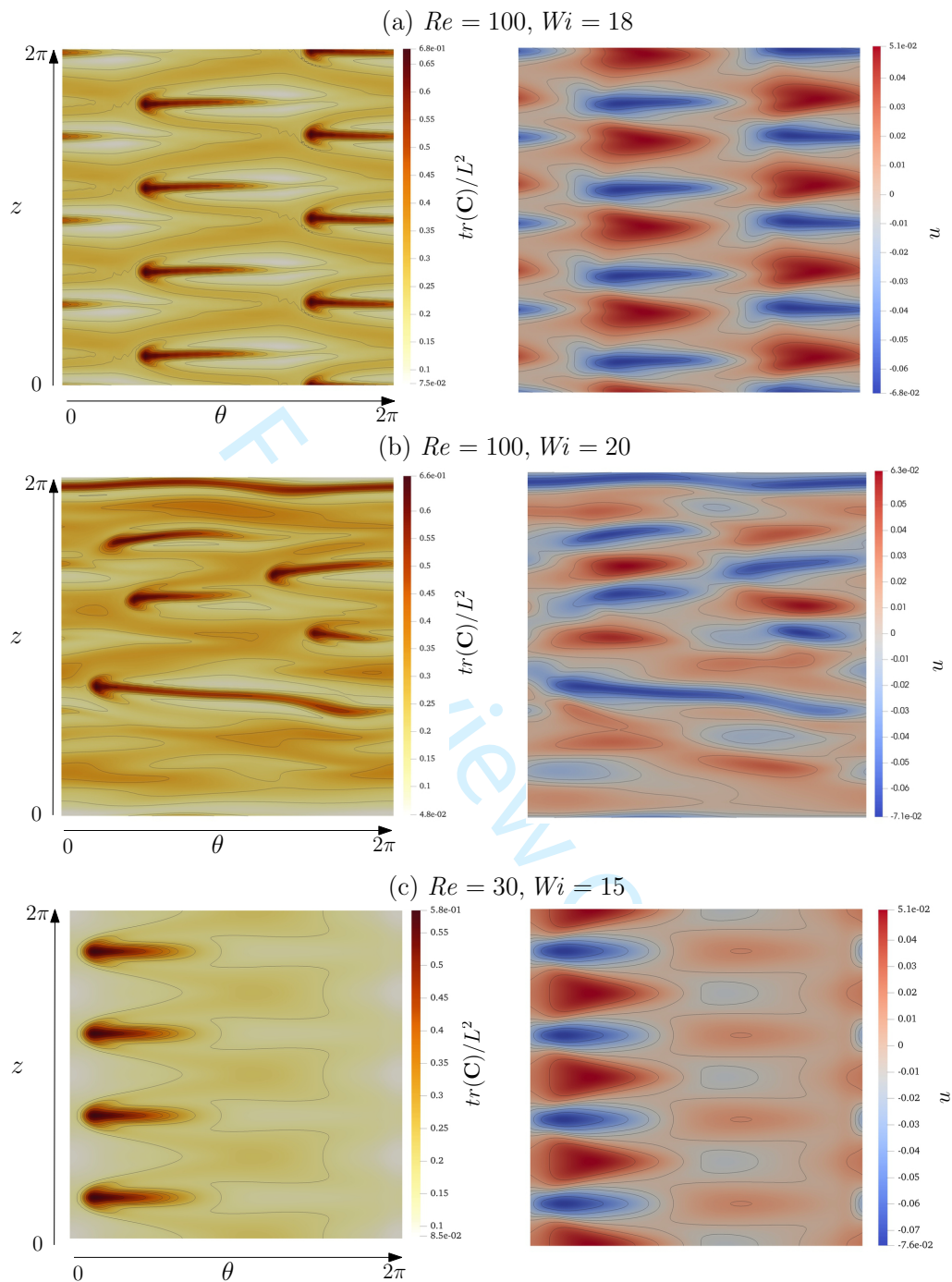
(c) $Re = 30$, $Wi = 15$

Figure 7. (Color online) Colour maps of the polymer stretch field (left panels) and radial velocity (right panels) illustrating other flow states where arrow-shaped structures of polymer stretch are also observed. (a) AArrowRW for $Re= 100$ and $Wi= 18$, (b) DO for $Re= 100$ and $Wi= 20$ and (c) LArrowRW for $Re= 30$, and $Wi= 15$. As in the previous figures, a cylindrical section (θ, z) obtained at the mid-gap is shown in each panel. Eight contours evenly spaced across the entire range of values (indicated in the colorbar) are shown in each case. The flow direction is from left to right.

Submitted to Phil. Trans. R. Soc. A - Issue

Page 16 of 34

the cylindrical sections presented in this paper. This characteristic could hence be used to detect these structures in experiments.

Despite its age and extensive research, the classical TCF setup (inner cylinder rotating and outer cylinder at rest) offers a great opportunity to detect previously unknown states. This is especially true when non-Newtonian fluids, such as viscoelastic fluids, are used as working fluids, further expanding the problem's already large parameter space.

Authors' Contributions. 'J.M.L and S.A. carried out the simulations, performed the data analysis and wrote the manuscript'.

References

1. Taylor, G. I. 1923. Stability of a viscous liquid contained between two rotating cylinders *Philos. Trans. R. Soc. Lond. A* **223** 289.
2. Andereck, C. D. Liu, S. S. and Swinney, H. L. 1986. Flow regimes in a circular Couette system with independently rotating cylinders. *J. Fluid Mech.* **164**, 155.
3. Chossat, P. & Iooss, G. 1994. *The Couette-Taylor Problem* Springer, Berlin.
4. Tagg, R. 1994. *The Couette-Taylor Problem* Nonlinear Sci. Today **4**, 1.
5. Langford, W. F., Tagg, R., Kostelich, E. J., Swinney, H. L. and Golubitsky, M. 1988. Primary instabilities and bicriticality in flow between counter rotating cylinders. *Phys. Fluids* **31**, 776-785.
6. Jones, C. A. 1981. Nonlinear Taylor vortices and their stability. *J. Fluid Mech.* **102**, 249–261.
7. Jones, C. A. 1985. The transition to wavy Taylor vortices. *J. Fluid Mech.* **157**, 135–162.
8. King, G. P., Lee, Y. Li, W., Swinney, H. L. and Marcus, P. S. 1984. Wave speeds in wavy Taylor-vortex flow. *J. Fluid Mech.* **141**, 365–390.
9. Wereley, S. T. and Lueptow, R. M. 1998. Spatio-temporal character of non-wavy and wavy Taylor–Couette flow. *J. Fluid Mech.* **364**, 59–80.
10. Martinand, D., Serre, E. and Lueptow, R. M. 2014. Mechanisms for the transition to waviness for Taylor vortices. *Phys. Fluids* **26**,(9), 094102.
11. Dessup, T., Tuckerman, L. S., Wesfreid, J. E., Barkley, D. and Willis, A. P. 2018. Self-sustaining process in Taylor-Couette flow. *Phys. Rev. Fluids* **3**, 123902.
12. Andereck, C. D., Liu, S. S. and Swinney, H. L. 1986. Flow regimes in a circular Couette system with independently rotating cylinders. *J. Fluid Mech.* **164**, 155-183.
13. Lacassagne, T., Cagney, N. and Balabani, S. 2021. Shear-thinning mediation of elasto-inertial Taylor–Couette flow. *J. Fluid Mech.* **915**, A91.
14. Lacassagne, T., Cagney, N., Gillissen, J. J. J. and Balabani, S. 2020. Vortex merging and splitting: A route to elastoinertial turbulence in Taylor-Couette flow. *Phys. Rev. Fluids* **5**, 113303.
15. Cagney, N., Lacassagne, T. and Balabani, S. 2020. Taylor–Couette flow of polymer solutions with shear-thinning and viscoelastic rheology. *J. Fluid Mech.* **905**, A28.
16. Lopez Jose. M. 2022. Vortex merging and splitting events in viscoelastic Taylor–Couette flow. *J. Fluid Mech.* **946**, A27.
17. Latrache, N. and Mutabazi, I. 2021. Transition to turbulence via flame patterns in viscoelastic Taylor–Couette flow. *Eur. Phys. J. E Soft Matter* **44** (5), 63.
18. Muller, S. J., Larson, R. G. and Shaqfeh, E. S. 1989. A purely elastic transition in Taylor-Couette flow. *Rheologica Acta* **28** (6), 499–503.
19. Larson, R. G., Shaqfeh, E. S. G. and Muller, S. J. 1990. A purely elastic instability in Taylor–Couette flow. *Journal of Fluid Mechanics* **218**, 573–600.
20. Shaqfeh, E. S. G. 1996 Purely elastic instabilities in viscometric flows. *Annu. Rev. Fluid Mech.* **28** (1), 129–185.
21. Groisman, A. and Steinberg, V. 1996. Couette-Taylor flow in a dilute polymer solution. *Phys. Rev. Lett.* **77**, 1480–1483.

15

Page 17 of 34

Submitted to Phil. Trans. R. Soc. A - Issue

22. Crumeyrolle, O., Mutabazi, I. and Grisel, M. 2002. Experimental study of inertioelastic Couette–Taylor instability modes in dilute and semidilute polymer solutions. *Phys. Fluids* **14** (5), 1681–1688.

23. Thomas, D. G., Khomami, B. and Sureshkumar, R. 2009. Nonlinear dynamics of viscoelastic Taylor–Couette flow: effect of elasticity on pattern selection, molecular conformation and drag. *J. Fluid Mech.* **620**, 353–382.

24. Thomas, D. G., Sureshkumar, R. and Khomami, B. 2006. Pattern formation in Taylor-Couette flow of dilute polymer solutions: Dynamical simulations and mechanism. *Phys. Rev. Lett.* **97**, 054501.

25. Latrache, N., Abcha, N., Crumeyrolle, O. and Mutabazi, I. 2016. Defect-mediated turbu- lence in ribbons of viscoelastic Taylor-Couette flow. *Phys. Rev. E* **93**, 043126.

26. Groisman, A. and Steinberg, V. 1997. Solitary vortex pairs in viscoelastic Couette flow. *Phys. Rev. Lett.* **78**, 1460–1463.

27. Baumert, B. M. and Muller, S. J. 1997. Flow regimes in model viscoelastic fluids in a circular Couette system with independently rotating cylinders. *Phys. Fluids* **9** (3), 566–586.

28. Baumert, B. M. and Muller, S. J. 1999. Axisymmetric and non-axisymmetric elastic and inertio-elastic instabilities in Taylor–Couette flow. *J. Nonnewton. Fluid Mech.* **83** (1), 33–69.

29. Liu, N. and Khomami, B. 2013. Elastically induced turbulence in Taylor–Couette flow: direct numerical simulation and mechanistic insight. *J. Fluid Mech.* **737**, R4.

30. Song, J., Lin, F., Liu, N., Lu, X.-Y. and Khomami, B. 2021a. Direct numerical simulation of inertio-elastic turbulent Taylor–Couette flow. *J. Fluid Mech.* **926**, A37.

31. Song, J., Teng, H., Liu, N., Ding, H., Lu, X.-Y. Khomami, B. 2019 The correspondence between drag enhancement and vortical structures in turbulent Taylor–Couette flows with polymer additives: a study of curvature dependence. *J. Fluid Mech.* **881**, 602–616.

32. Page, J., Dubief, Y. and Kerswell, R. R. 2020. Exact traveling wave solutions in viscoelastic channel flow. *Phys. Rev. Lett.* **125**, 154501.

33. Dubief, Y. and Page, J. and Kerswell, R. R. and Terrapon, V. E. and Steinberg, V. 2022. First coherent structure in elasto-inertial turbulence. *Phys. Rev. Fluids* **7** (7), 073301.

34. Samanta, D. Dubief, Y. Holzner, M. Schäfer, C. Morozov, A. N. *et al.* 2013. Elasto-inertial turbulence. *PNAS* **110**, 10557-62.

35. Dubief, Y. Terrapon, V. E. Soria, J. 2013. On the mechanism of elasto-inertial turbulence. *Phys. Fluids* **25** 110817.

36. Sid, S. Terrapon, V. E. Dubief Y. 2018. Two-dimensional dynamics of elasto-inertial turbulence and its role in polymer drag reduction. *Phys. Rev. Fluids* **3** 011301.

37. Shekar, A. McMullen, R. M. Wang, S. N. McKeon, B. J. Graham, M. D. 2019b. Critical-layer structures and mechanisms in elastoinertial turbulence. *Phys. Rev. Lett.* **122** 124503.

38. Bird, R., Dotson, P. and Johnson, N. 1980. Polymer solution rheology based on a finitely extensible bead—spring chain model. *J. Nonnewton. Fluid Mech.* **7** (2), 213 – 235.

39. Liu, N. and Khomami, B. 2013. Elastically induced turbulence in Taylor–Couette flow: direct numerical simulation and mechanistic insight. *J. Fluid Mech.*, **737**, R4.

40. Song, J., Lin, F., Liu, N., Lu, X.-Y. and Khomami, B. 2021. Direct numerical simulation of inertio-elastic turbulent Taylor–Couette flow. *J. Fluid Mech.*, **926**, A37.

41. Song, J., Teng, H., Liu, N., Ding, H., Lu, X.-Y. and Khomami, B. 2019. The correspondence between drag enhancement and vortical structures in turbulent Taylor–Couette flows with polymer additives: a study of curvature dependence. *J. Fluid Mech.*, **881**,602–616.

42. Song, J., Wan, Z.-H., Liu, N., Lu, X.-Y. and Khomami, B. 2021b. A reverse transition route from inertial to elasticity-dominated turbulence in viscoelastic Taylor–Couette flow. *J. Fluid Mech.* **927**, A10.

43. Lopez, J. M., Feldmann, D., Rampp, M., Vela-Martin, A., Shi, L. and Avila, M. 2020 nsCouette–a high-performance code for direct numerical simulations of turbulent Taylor–Couette flow. *SoftwareX* **11**, 100395.

44. Lopez, J. M., Choueiri, G. H. and Hof, B. 2019 Dynamics of viscoelastic pipe flow at low Reynolds numbers in the maximum drag reduction limit. *J. Fluid Mech.*, **874**, 699–719.

45. Willis, A. P. 2017 The openpipeflow Navier–Stokes solver. *SoftwareX* **6**, 124 – 127.

46. Groisman, A. and Steinberg, V. 1998 Mechanism of elastic instability in Couette flow of polymer solutions: Experiment. *Phys. Fluids* **10** (10), 2451–2463.

47. Buza, G., Page, J. and Kerswell, R. 2022. Weakly nonlinear analysis of the viscoelastic instability in channel flow for finite and vanishing Reynolds numbers. *J. Fluid Mech.*, 940, A11

Submitted to Phil. Trans. R. Soc. A - Issue

Page 18 of 34

48. Choueiri, G. H., Lopez, J. M., Varshney, A., Sankar, S. and Hof, B. 2021. Experimental observation of the origin and structure of elastoinertial turbulence. *Proc. Natl. Acad. Sci. U.S.A.*, **118** (45), e2102350118.

49. Itano, T. and Toh, S. 2001 The dynamics of bursting process in wall turbulence. *J. Phys. Soc. Japan* **70** (3), 703–716.

50. Dallas, V. and Vassilicos, J. C. and Hewitt, G. F. 2010. Strong polymer-turbulence interactions in viscoelastic turbulent channel flow. *Physical Review E*, **82**, (6), 066303.

17

Page 19 of 34

Submitted to Phil. Trans. R. Soc. A - Issue

1
2
3
4
5
6
7
8
9
10
11
12
13
14
15
16
17
18
19
20
21
22
23
24
25
26
27
28
29
30
31
32
33
34
35
36
37
38
39
40
41
42
43
44
45
46
47
48
49
50
51
52
53
54
55
56
57
58
59
60

Author for correspondence:

Sebastian A. Altmeyer

e-mail:

sebastian.andreas.altmeyer@upc.edu

Arrow-shaped elasto-inertial rotating waves

Jose M. Lopez[1], Sebastian A. Altmeyer[1]

[1] Department of Fisica Aplicada, Universitat Politècnica de Catalunya, Girona s/n, Modul B4 Campus Nord, 08034 Barcelona, Spain

We present direct numerical simulations of the Taylor–Couette flow of a dilute polymer solution when only the inner cylinder rotates and the curvature of the system is moderate ($\eta = 0.77$). The finitely extensible nonlinear elastic-Peterlin (FENE-P) closure is used to model the polymer dynamics. The simulations have revealed the existence of a novel elasto-inertial rotating wave characterized by arrow-shaped structures of the polymer stretch field aligned with the streamwise direction. This rotating wave pattern is comprehensively characterized, including an analysis of its dependence on the dimensionless Reynolds and Weissenberg numbers. Other flow states having arrow-shaped structures coexisting with other types of structures have also been identified for the first time in this study and are briefly discussed.

2

1. Introduction

In the century that has elapsed since the pioneering work of G. I. Taylor [1], the Taylor–Couette flow (TCF), i.e. the fluid flow contained in the annular gap between two vertical concentric cylinders, has become one of the most prominent models for investigating flow pattern formation, instabilities, and turbulence in rotating shear flows [3–5,12]. This popularity has been partly motivated by the fact that, in many configurations of this system, the transition to the turbulence is supercritical, i.e. it occurs through a well-defined sequence of linear instabilities to flow patterns of increasing spatio-temporal complexity eventually leading to turbulence. The specific characteristics of these flow patterns depend crucially on the geometry of the apparatus (the curvature and the length-to-gap aspect ratio), the container boundaries and the relative rotation of the cylinders. However, it is frequently observed that the transition from axisymmetric to three-dimensional flow gives rise to waves that propagate in the azimuthal direction while keeping a constant shape. These flow states are known as rotating waves and appear when the system undergoes a Hopf bifurcation that breaks its SO(2) symmetry. The best-known example of a rotating wave pattern is the so-called wavy vortex flow, which emerges from the Taylor vortices as the inner cylinder rotation speed increases for a wide range of curvatures and aspect ratios [6–11]. Another well-studied example of rotating waves in pure hydrodynamic TCF is the Ribbons pattern (RB), which emerges when the cylinders counter-rotate [12].

While TCF has traditionally been studied using Newtonian fluids, a growing interest has been shown recently in investigating Non-Newtonian cases, especially when the working fluid is a dilute polymer solution. Due to their viscoelastic properties, long-chain polymers (even in small amounts) may substantially change the stability and spatio-temporal characteristics of the flow with respect to those in the Newtonian case. First observations of such phenomenon date back to about thirty years, with the detection of flow instability in the absence of inertia [18–20]. These studies were followed by a number of experimental works that explored in detail the formation of flow patterns depending on the relative importance between inertial and elastic effects [21,22,26–28]. A wide range of flow patterns was discovered, in many cases coexisting for the same values of the control parameters (the Reynolds and Weissenberg numbers), and it was concluded that observing one or more flow states was highly sensitive to polymer properties, initial conditions, and experimental protocol. One of the most typical states reported in these studies was the RB pattern, a rotating wave formed by two (symmetry degenerated) spiral waves that propagate axially in opposite senses [21,22]. As for Newtonian cases, viscoelastic RB arise from a supercritical Hopf bifurcation of the Circular Couette flow (CCF), but unlike Newtonian fluids, it is not necessary that the cylinders counter-rotate (they are observed even in the classical setup, where only the inner cylinder rotates). Depending on the flow's elasticity, they may occur at rotation speeds one order of magnitude smaller than those at which rotating waves exist in isothermal Newtonian TCF, and they have been found to play a major role in several transition routes to elasto-inertial turbulence (EIT) [17,25]. Other coherent states which are frequently encountered in experiments on TCF of a dilute polymer solution are diwhirls (DW), oscillatory strips (OS), disordered oscillations (DO) or flames (FL) [21,22,26–28]. However, unlike RB, the transition to these flow states, which may occur either from CCF or RB, is abrupt and highly hysteretic.

These coherent states could not be replicated in simulations until the late 2000s [23,24]. The use of the FENE-P (Finite extensibility nonlinear elastic-Peterlin) closure was critical to the success of these simulations because it included important effects of the polymer's finite extensibility that had been previously overlooked in numerical works. In addition to demonstrating the ability of the FENE-P model to accurately simulate polymer dynamics, the authors detailed the spatio-temporal characteristics of the flow states they discovered. However, because the parameter space was not thoroughly explored, there could be many more coherent states than

Page 21 of 34

Submitted to Phil. Trans. R. Soc. A - Issue

those reported in these studies. Since then, there has been a growing interest in studies aimed at characterizing elasto-inertial turbulence (EIT) [29–31] and no further studies (both numerical and experimental) on flow pattern formation and transition to the EIT have been performed until very recently [13–17,42]. Given the problem's large parameter space, the large number of states that can coexist for the same values of the control parameters, and the scarcity of numerical studies on viscoelastic flow patterns, it is reasonable to expect previously unreported states to emerge in numerical studies on these flows.

Whereas for TCF, coherent elasto-inertial flow patterns have been studied for nearly three decades, for parallel shear flows, only recently the first coherent viscoelastic structure has been found in simulations of a two-dimensional channel flow [32,33]. These structures are travelling waves (the analogue of the rotating waves in parallel flows) that propagate downstream at a speed close to the centreline velocity. The hallmark of these viscoelastic travelling waves is the existence of arrowhead structures in the polymer stretch field which are oriented in the streamwise direction. It has been speculated that these structures may be caused by an increase in the elongational viscosity of the fluid due to polymer stretching in the flow direction [33]. This characteristic suggests that these arrow-shaped structures of polymer stretch may not be exclusive to parallel shear flows, but a universal feature of flow systems where polymers are subjected to elongational flow. In TCF, for instance, polymers are stretched by the primary flow in the azimuthal direction. Hence, an increase in the fluid's elongational viscosity might result in arrow-shaped structures aligned with the azimuthal direction. However, as far as we are aware, no evidence of these structures in flows with curved streamlines has been reported yet.

In this paper, using direct numerical simulations of the TCF of a dilute polymer solution, where the FENE-P closure is used to model the polymer dynamics, we show that arrow-shaped structures of polymer stretch aligned with the streamwise direction (in this case the azimuthal direction) also exist in TCF. These structures are identified in elasto-inertial rotating waves that propagate with a very slow frequency and in chaotic states. We determine the range of existence of the rotating wave solutions in the parameter space defined by the dimensionless Reynolds and Weissenberg numbers and show how the characteristics of the arrow-shaped structures change as these parameters are varied. We also briefly discuss other solution branches found in our study.

2. Problem formulation and methodology

(a) Governing equations and dimensionless parameters

We consider the flow of a dilute polymer solution driven in the annular gap between two vertical, rigid, and independently rotating cylinders of height h. The inner cylinder of radius r_i rotates at angular speed Ω_i and the outer cylinder of radius r_o is kept at rest, i.e. $\Omega_o = 0$. The fluid is incompressible and the dynamics is governed by the Navier-Stokes and continuity equations. An additional equation is needed to describe the temporal evolution of a polymer conformation tensor, $\mathbf{C}$, which contains the ensemble average elongation and orientation of all polymer molecules in the flow. Each polymer molecule is modeled by a finitely extensible elastic dumbbell [38]. The dimensionless equations read

$$\nabla \cdot \mathbf{v} = 0,$$

$$\partial_t \mathbf{v} + \mathbf{v} \cdot \nabla \mathbf{v} = -\nabla P + \frac{\beta}{Re} \nabla^2 \mathbf{v} + \frac{(1-\beta)}{Re} \nabla \cdot \mathbf{T}, \tag{2.1}$$

$$\partial_t \mathbf{C} + \mathbf{v} \cdot \nabla \mathbf{C} = \mathbf{C} \nabla \mathbf{v} + (\nabla \mathbf{v})^T \mathbf{C} - \mathbf{T},$$

where $\mathbf{v} = (u, v, w)$ is the velocity vector field in cylindrical coordinates (r, θ, z), P is the pressure, $\beta = \nu_s/\nu$ indicates the relative importance between the solvent viscosity, ν_s, and the viscosity of the solution at zero shear rate, ν. The length scale of the system is normalized with the gap width,

Submitted to Phil. Trans. R. Soc. A - Issue

Page 22 of 34

4

$d = r_o - r_i$, the velocity with the inner cylinder velocity, $\Omega_i r_i$, the pressure with the dynamic pressure, $\rho(\Omega_i r_i)^2$, where ρ is the fluid's density, and the polymer conformation tensor with $k_B T_e / H$, where k_B denotes the Boltzmann constant, T_e is the absolute temperature and H is the spring constant.

The coupling between the polymers and the Navier-Stokes equations is realized through the polymer stress tensor $\mathbf{T}$, which is calculated using the FENE-P model [38],

$$\mathbf{T} = \frac{1}{Wi}\left(\frac{\mathbf{C}}{1 - \frac{tr(\mathbf{C})}{L^2}} - \mathbf{I}\right), \qquad (2.2)$$

where $\mathbf{I}$ is the unit tensor, $tr(\mathbf{C})$ is the trace of the polymer conformation tensor, L denotes the maximum polymer extension parameter and Wi is the Weissenberg number (defined below).

Periodic boundary conditions are imposed in the z and θ directions, whereas the boundary conditions at the cylinders are

$$\mathbf{v}(r_i, \theta, z) = (0, 1, 0), \quad \mathbf{v}(r_o, \theta, z) = (0, 0, 0). \qquad (2.3)$$

The system is governed by the following independent non-dimensional parameters:

$$
\begin{aligned}
&\text{Reynolds number:} && Re = \Omega_i r_i d / \nu, \\
&\text{Weissenberg number:} && Wi = \lambda / [d/(\Omega_i r_i)] \\
&\text{Radius ratio:} && \eta = r_i / r_o, \\
&\text{Aspect ratio:} && \Gamma = h/d,
\end{aligned}
\qquad (2.4)
$$

where λ is the polymer relaxation time and $d/(\Omega_i r_i)$ is the advective time scale.

In this paper, the radius ratio and aspect ratio are fixed to $\eta = 0.77$ and $\Gamma = 2\pi$, respectively. A constant polymer concentration $\beta = 0.871$ is used and the maximum polymer extension parameter L is set to 100, in accordance with recent studies of elasto-inertial turbulence on viscoelastic TCF [16,39–41]. The flow's elasticity level, quantified by the elasticity number $El = Re/Wi$, ranges from 0.01 to 1. The parameter space is explored by either fixing Re and varying Wi or vice versa, and consequently, the value of El changes among simulations. This protocol differs from that in [23,24], the only numerical study on flow pattern formation in viscoelastic TCF conducted to date, where the simulations were performed at a constant El for five different El values ($El = 0.33$, $El = 0.50$, $El = 0.75$, $El = 1$ and $El = 30$). Another difference with respect to this study is the polymer concentration. The polymer solution used in our simulations is nearly 10% more diluted than that used in [23,24] ($\beta = 0.8$ in these references).

(b) Numerical methods

The governing equations (2.1) are solved with the open source code nsCouette [43]. The code is a combination of high-order central finite differences on a Gauss-Lobatto-Chebyshev grid in r and Fourier-Galerkin expansions in z and θ. Decoupling between pressure and velocity field is realized by a Pressure Poisson Equation formulation. The free divergence condition is enforced by using an influence matrix technique, so that this condition is satisfied up to machine error. A second-order accurate predictor-corrector scheme based on the Crank-Nicolson method is used to carry out the time integration (see references [44,45] for further details about the timestepper). Following the customary approach in numerical simulations of viscoelastic flows using pseudo-spectral codes, a small amount of artificial diffusion is added to stabilize the integration. The reason to include this diffusion is the hyperbolic nature of the time evolution equation for $\mathbf{C}$. In the absence of diffusion, integration of this equation often results in an accumulation of numerical error, which in many cases produce numerical breakdown. This issue can be overcome by adding a Laplacian term, $\frac{1}{ReS_c}\nabla^2 \mathbf{C}$, to the right-hand side of this hyperbolic equation, where the Schmidt number, $S_c = \nu/\kappa$, quantifies the ratio between the viscous and artificial diffusivities. In the simulations presented here, S_c has been varied between 50 and 100, so that the artificial diffusion

Page 23 of 34

Submitted to Phil. Trans. R. Soc. A - Issue

coefficient, $\frac{1}{ReSc_c}$, is of the order of 10^{-4}. Several tests using larger Sc values (Sc up to 200 were tested) have been conducted to verify that further reduction in the diffusion coefficient does not alter significantly the results of the simulations. The number of radial nodes and Fourier modes used in the computations were $m_r = 64$, $m_\theta = 33$ and $m_z = 256$, whereas the time step size was set to 5×10^{-3}.

3. Arrow shaped structures of polymer stretch

To probe whether arrow-shaped structures of polymer stretch exist in viscoelastic TCF, we have conducted simulations at low Re values ($Re \leq 100$) while keeping $Wi = 15$. The elasticity number, $El = Wi/Re$, in these simulations falls within the range $0.15 \leq El \leq 0.75$, which is consistent with the elasticity levels at which arrowhead structures have been observed in channels. The simulations were started from the laminar state, previously computed, which was perturbed by a disturbance of the form,

$$u = A(r - r_i)(r - r_o)cos(\theta + kz) \tag{3.1}$$

$$w = -A\frac{(r - r_i)(r - r_o)}{r}(5r^2 - 3(r_i + r_o)r + r_i r_o)\frac{sin(\theta + kz)}{k}, \tag{3.2}$$

where k is the axial wavenumber and A denotes the amplitude of the perturbation. If the value of A is sufficiently large, the simulations converge to a rotating wave with azimuthal wavenumber m=1. The amplitude threshold required to cause the instability is small (it can be as small as $A \sim O(10^{-8})$ at the largest Re investigated), yet below this threshold the energy of the perturbation decays and the laminar state persists. This indicates that these rotating wave patterns are driven by nonlinear effects. We note that the existence of subcritical instabilities triggered by very low amplitude thresholds is consistent with recent findings in other studies on viscoelastic flows at low Reynolds numbers [47,48]. Depending on the value of k used in the initial condition, flow patterns with three or four pairs of counter-rotating vortices were obtained. In the following, we will restrict the discussion to the case where the flow pattern has four vortex pairs.

The upper panels of figure 1 show colour maps of the trace of the polymer conformation tensor, $tr(\mathbf{C})$, normalized with the maximum elongation of the polymers, L^2, in a cylindrical section (θ,z) at three different radial locations (indicated on top of each panel) for a simulation conducted at $Re= 90$. This quantity indicates the degree of stretching of the polymer chains. High values of $tr(\mathbf{C})/L^2$ (dark regions) denote highly stretched polymers, whereas low values of $tr(\mathbf{C})/L^2$ (lighter regions) indicate that polymers are weakly stretched. As is evident from the figure, the most distinctive feature of this flow state is the existence of regions of highly stretched polymers in the shape of an arrow. Due to this characteristic, it will be hereafter referred to as arrow-shaped rotating wave (ArrowRW). These arrow-shaped structures are observed across the radial gap, except for the regions very close to the cylinders, but their shapes differ depending on the radial location. As one moves from the outer to the inner cylinder (from right to left in the figure), the body of the arrow progressively shortens, and the axial extent of the arrowhead increases.

To illustrate the correspondence between polymer stretch and flow velocity, the lower panels of the figure 1 show colour maps of the radial velocity in the same section and at the same time instant as the upper panels. Positive velocity (red areas) denotes fluid motion from the inner to the outer cylinder, i.e outflows, whereas negative velocity (blue areas) indicates fluid moving from the outer to the inner cylinder, i.e. inflows. When the upper and lower rows of the figure are compared, it becomes evident that the arrow-shaped structures of highly stretched polymers are associated with inflow regions, whereas outflows occur in areas where the polymer stretch is lower (less than 25% of L^2). The wake of the arrows, on the other hand, corresponds to the vicinity of the boundaries between inflows and outflows, where the radial velocity is close to zero. As seen, the velocity in the inflows is higher than that of the outflows. This characteristic is caused by the elastic force created by the stretched polymers. This force acts radially inward
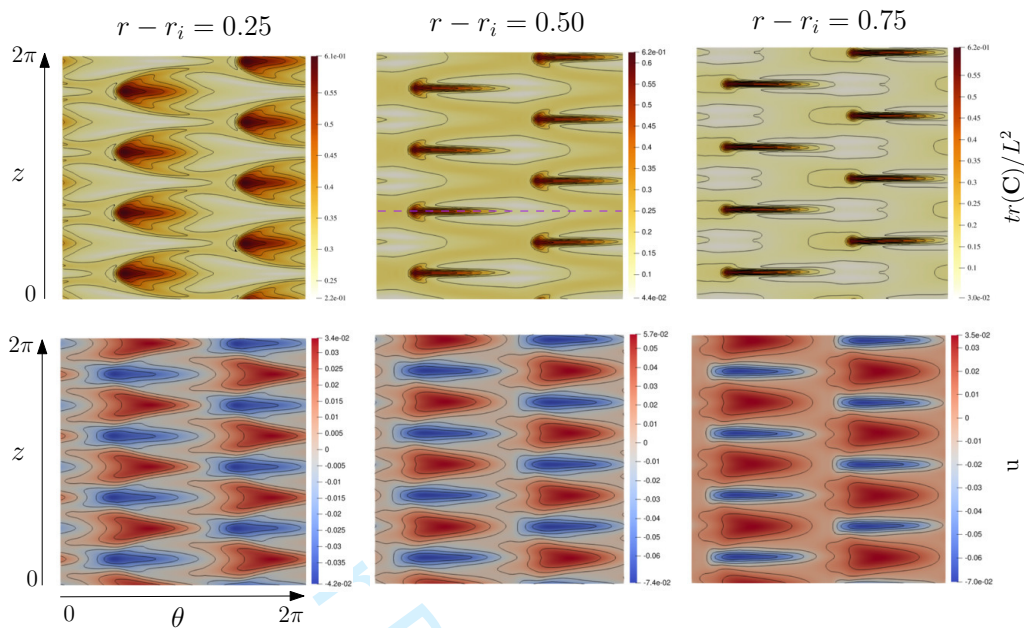
Submitted to Phil. Trans. R. Soc. A - Issue

Page 24 of 34

Figure 1. (Color online) The upper panels show colour maps of the trace of the polymer conformation tensor, $tr(\mathbf{C})$, normalized with the maximum polymer extension, L^2, in cylindrical sections (θ, z) at three different radial locations. Dark (light) regions indicate regions where polymers are highly (slightly) stretched. The lower panels display colour maps of the radial velocity, u, at the same time instant and in the same cylindrical sections as the upper panels. Red (blue) areas indicate outflows (inflows). The example shown corresponds to a snapshot of a simulation with $Re = 90$, $L = 100$, $\beta = 0.871$, and $Wi = 15$. Eight contours evenly spaced across the entire range of values (indicated in the colorbar) are shown in each case. The flow direction is from left to right.

and hence enhances fluid motion through the inflows while slowing down the motion through the outflows. This creates an asymmetry between inflows and outflows (the axial extent of the outflows is larger than that of the inflows) which has been discussed in detail in [46] and [16]. The highest degree of asymmetry occurs near the outer cylinder, where the elastic force exhibits strong localized peaks that result in strong localized inflow jets (note that the axial extent of the outflow regions here is more than twice that of the inflow regions, see panel corresponding to $r - r_i = 0.75$). However, as we move towards the inner cylinder, the magnitude of the elastic force decays gradually, and consequently, the degree of asymmetry between inflows and outflows also diminishes (see panels for $r - r_i = 0.50$ and $r - r_i = 0.25$). The changes observed in the arrow-shaped structures when these are plotted at distinct radial locations (upper panels) can thus be ascribed to the radial dependence of the elastic force and how this modifies the axial extent of the inward motion.

To provide a simpler quantitative characterization of the polymer stretch, we show in figure 2 the variation of $tr(\mathbf{C})/L^2$ along the azimuthal direction at fixed radial (mid-gap) and axial ($z = 2.25$) locations for the same snapshot shown in figure 1 (i.e. along the purple dashed line shown in that figure). We note that the same plot is obtained if $tr(\mathbf{C})/L^2$ is plotted as a function time at a fixed azimuthal location (time is shown in the upper abscissa of the figure). This happens because in rotating waves the variation in θ is commensurate with the temporal evolution of the flow pattern. Figure 2 shows that the emergence of the arrow-shaped structures is associated with an abrupt local increase of $tr(\mathbf{C})/L^2$. The maximum value of $tr(\mathbf{C})/L^2$ is achieved in the head of the arrow, shortly after the sudden increase takes place, and it can be as large as 0.75 (i.e. 75% of the maximum polymer elongation) for the largest values of Re and Wi simulated in this study.
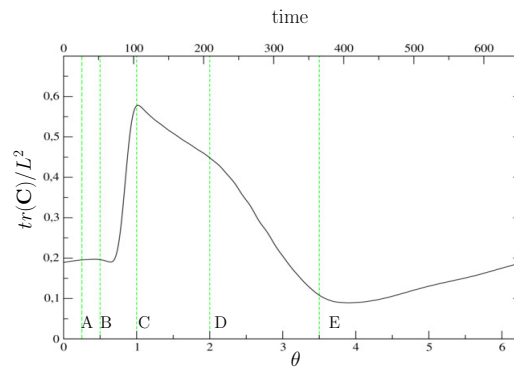
Figure 2. Trace of the polymer conformation tensor, normalized by L^2, obtained at the mid-gap ($r - r_i = 0.5$)and $z/d = 2.25$ as a function of θ (lower abscissa) and time (upper abscissa). The values of θ for which meridional sections are shown in figure 3 are represented as green dashed lines.

The decay of $tr(\mathbf{C})/L^2$ exhibits two phases: a slow decay that coincides with the body of the arrow and a sharper decay that occurs in the wake behind the arrow ($2 < \theta < 3.5$). The minimum value of $tr(\mathbf{C})/L^2$ is reached in the latter region and it is in all simulations lower than 10% of the maximum polymer elongation. After the minimum, $tr(\mathbf{C})/L^2$ increases gradually until it reaches a value of nearly 0.2 which remains constant before the emergence of the arrow-shaped structure.

We finally show in figure 3 the radial dependence of the polymer stretch (upper row) and flow streamlines (lower row) as a function of θ. The values of θ at which snapshots are displayed are shown as dashed lines in figure 2. The leftmost panels (A, $\theta = 0.25$) illustrate the flow upstream of the arrow-shaped structure, far from the arrowhead. Polymers here are more stretched in the region near the inner cylinder. This circumstance appears to be related to the emergence of flow recirculation zones near the inner cylinder (see the leftmost panel of the lower row), which displace the main vortices towards the outer cylinder. As the arrowhead is approached, the intensity of the vortices increases and the recirculating vortices near the inner cylinder weaken. As a result, polymers get increasingly more stretched near the outer cylinder (see panels B, for $\theta = 0.5$). Jets of highly stretched polymers emanate then from the outer cylinder and move towards the inner cylinder through the inflows (see panels C, which corresponds to the arrowhead, $\theta = 1$). Vigorous counter-rotating vortex pairs, with a clear asymmetry between inflows and outflows, as described above, extend across the entire radial gap (lower C panel). This situation continues as one moves toward the bottom end of the arrow-shaped structure. When the jet of highly stretched polymers meets the inner cylinder, it begins to spread along the wall (see panel D, for $\theta = 2$), and polymers get progressively more stretched in this region. The initial situation where the recirculations zones appear near the inner cylinder and the vortices move towards the outer cylinder is eventually recovered (see panel E, for $\theta = 3.5$) and the cycle starts again (with the vortices and regions of highly stretched polymers shifted by half a wavelength with respect to the first half of the rotation period).

4. *Re* and *Wi* parameter dependence

To establish the range of existence of the ArrowRW solution in the *Wi-Re* parameter space and how the characteristics of the arrow-shaped structures change with varying these parameters, we have conducted natural continuation of this flow state. The black line in figure 4 (a) shows the deviation of the volume averaged kinetic energy, k_e, with respect to its laminar value, for the ArrowRW state at the *Re* values at which this solution is found when *Wi*= 15. We note that
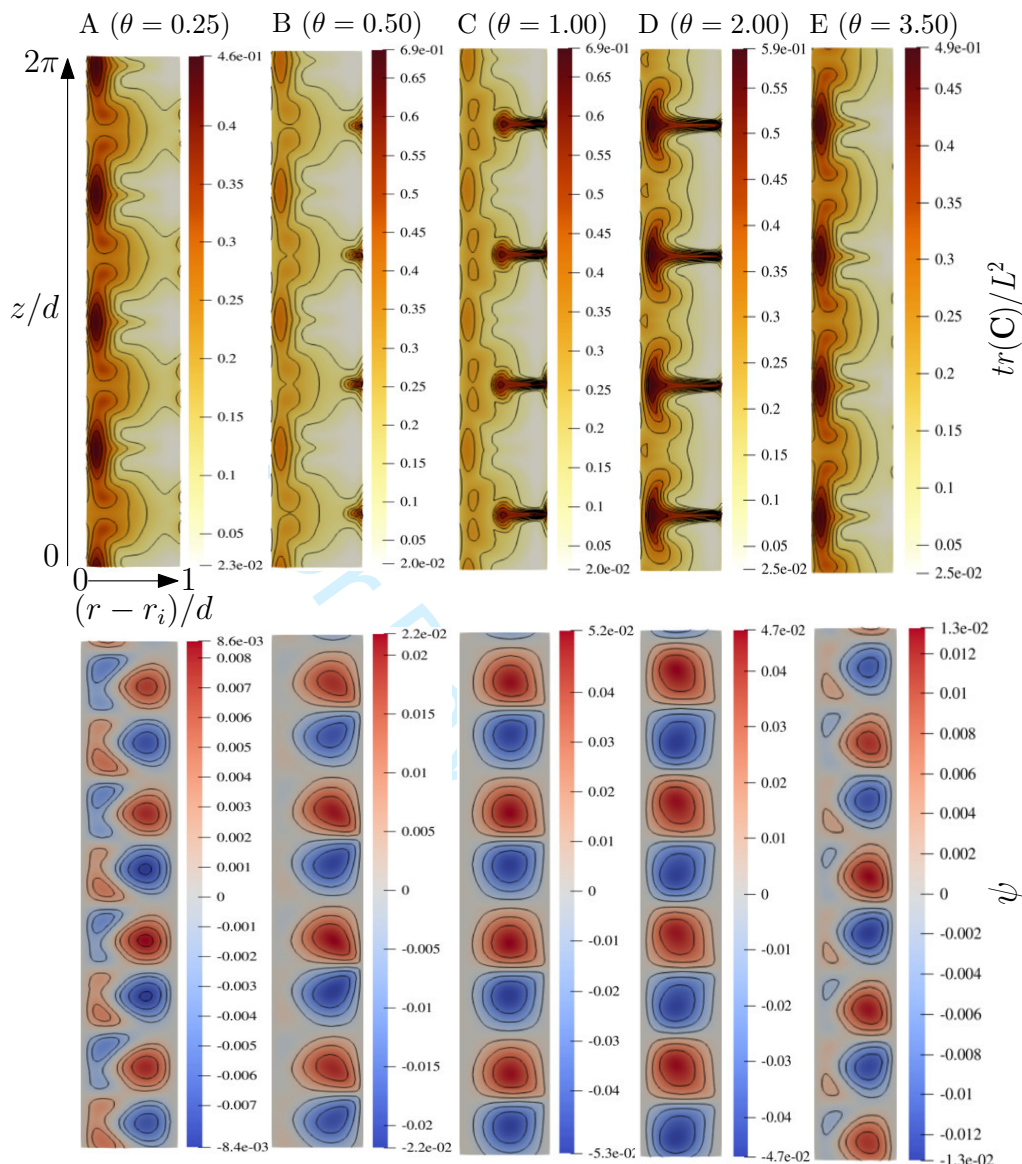
Submitted to Phil. Trans. R. Soc. A - Issue

Page 26 of 34

Figure 3. (Color online) Colour maps of polymer stretch (upper row) and flow streamlines ψ (lower row) shown in meridional sections (r, z) obtained at the values of θ indicated at the top of each panel (and shown as dashed (green) lines in the figure 1). Eight contours evenly spaced across the full range of values have been added to each panel.

for this Wi value, the base flow is linearly stable. The ArrowRW solution vanishes at a saddle-node bifurcation that takes place at $Re \approx 20$. It should be noted that this value of Re is well below that at which Taylor vortices appear in the Newtonian case ($Re \approx 90$), clearly showing that the instability relies on the interplay between inertia and elasticity. The lower branch solution that continues at lower energy towards larger Re values is unstable, but it could be detected by using the bisection method introduced by [49] (see black dashed line in figure 4 (a)). Only a few points of this solution branch have been computed, as flow states here are characterized by very weakly stretched polymers and arrow-shaped structures are no longer observed. To follow the ArrowRW solution branch near the saddle-node, it is necessary to vary Re in very small steps. If the change in Re is too large, the simulations converge to a different flow state, labeled LArrowRW in the

Page 27 of 34

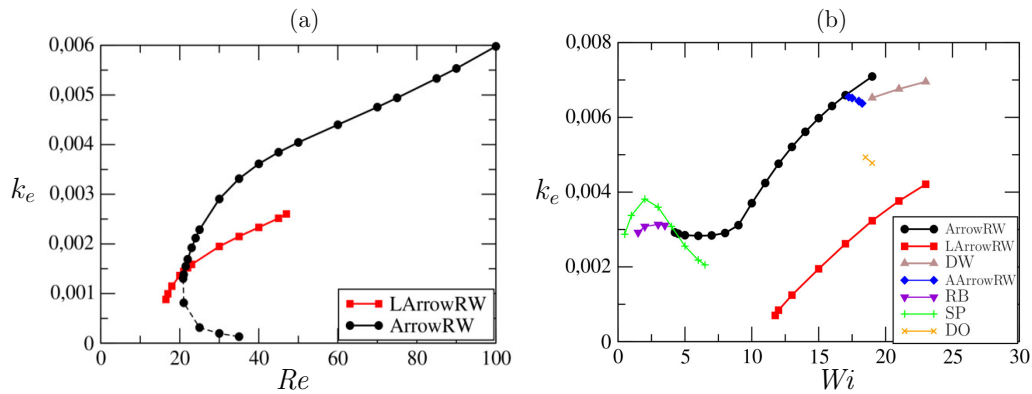Submitted to Phil. Trans. R. Soc. A - Issue

Figure 4. (Color online) Variation of the deviation of the volume average kinetic energy in the flow states found in the present study as the *Re* and *Wi* numbers are varied. Note that the volume average kinetic energy corresponding to the laminar state has been subtracted. (a) *Re* number dependence when *Wi*$= 15$ and (b) *Wi* number dependence when *Re*$= 100$, except for the LArrowRW state where *Re*$= 30$. The acronyms shown in the legend stand for: arrow shaped rotating wave (ArrowRW), localized arrow-shaped rotating wave (LArrowRW), asymmetric arrow-shaped rotating wave (AArrowRW), spirals (SP), diwhirls (DW), ribbons (RB) and disordered oscillations (DO).

figure, which is characterized by azimuthally localized arrow-shaped structures (This state is illustrated in figure 7 (c) and described in more detail in section 5). The LArrowRW coexists with the ArrowRW for $20 \lessapprox Re \lessapprox 45$, and it could be followed up to $Re \approx 16.5$, a value slightly lower than that at which the ArrowRW disappears. Below this threshold, the flow laminarises.

The highest *Re* value at which the ArrowRW exists for *Wi*$= 15$ is *Re*$= 100$. With further increase in *Re*, the flow pattern begins to exhibit additional modulations and complex spatio temporal dynamics set in. These states are, however, outside the scope of this paper and will be discussed elsewhere. As expected, polymer stretch increases with increasing *Re* due to the increase in the magnitude of the mean azimuthal velocity, reaching a maximum value of 75% of L^2 for *Re*$= 100$. The upper row of the figure 5 shows colour maps of the polymer stretch in a cylindrical section at the mid-gap for the simulations performed at *Re*$= 25$ and *Re*$= 50$. Along with the middle panel in the upper row of figure 1, for *Re*$= 90$, these figures illustrate the variation of the structures of polymer stretch as the *Re* number increases along the upper branch solution while holding the *Wi* number constant. For *Re* values near the saddle-node bifurcation (see panel for *Re*$= 25$), the arrow-shaped structures are not yet evident. The maximum polymer stretch here is still rather moderate (less than 50% of the maximum polymer extension) and this results in oval-shaped structures, where the azimuthal extent is only slightly larger than the axial extent (see darker zones). As *Re* increases and the stretching of the polymers increases, the structures become increasingly more elongated in the azimuthal direction and the arrow shape emerges. The right upper panel of the figure 5 shows that for *Re*$= 50$, the arrow-shaped structures can be already clearly distinguished, even though the highest polymer stretch is still not too large (only slightly above half of L^2).

The black line in figure 4 (b) illustrates the variation of the ArrowRW state when *Re*$= 100$ and *Wi* is varied. The minimum *Wi* number at which the solution could be followed is *Wi*$= 4.25$. Below this threshold, the ArrowRW becomes unstable and simulations converge to either RB or Spirals (SP). Two distinct trends are observed in the energy of the ArrowRW. It remains nearly constant when $4.25 \leq Wi \leq 9$ and increases with increasing *Wi* when *Wi*> 9. Despite the transition between the two regimes appearing to be rather smooth, the flow structures are qualitatively and quantitatively very different. Whereas for large *Wi* numbers, the arrow-shaped structures of highly stretched polymers shown in the figure 1 are observed, in the regime where the energy
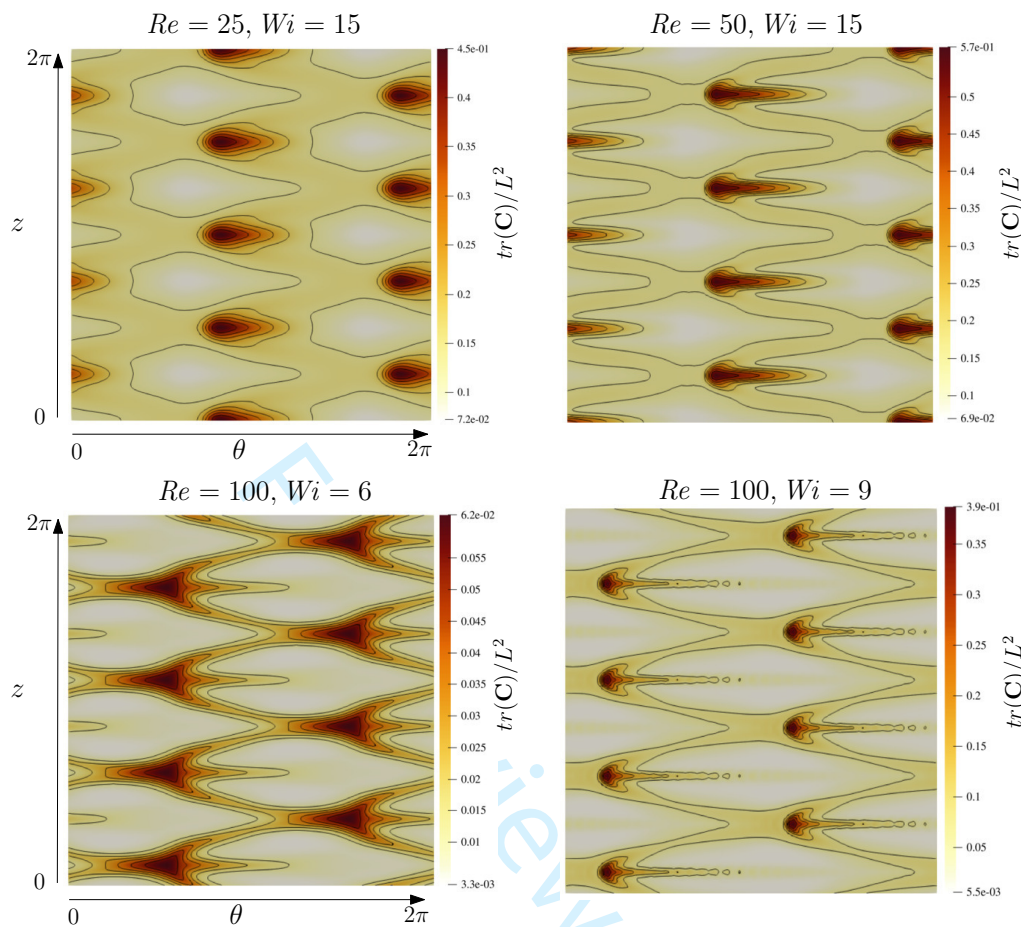
Figure 5. (Color online) Variation of the structures of polymer stretch as the *Re* (upper row) and *Wi* (lower) numbers are varied. Cylindrical sections (θ,z) obtained at the mid-gap are shown. Eight contours evenly spaced across the full range of values have been added to each panel.

is almost constant, the structures of polymer stretch take the form of a fork oriented in the flow direction (see left panel of figure 5 for *Wi*= 6). Interestingly, the amount of polymer stretch in these structures is surprisingly low (below 10% of L^2). It must be noted that the simulation for *Wi*= 4.25 was run for nearly 10000 advective time units. The solution persisted for this time and there was not any sign that there could be a change in the flow pattern with further simulation time. Hence, this surprising solution appears to be stable. As *Wi* increases, the forked-shaped structures are gradually replaced by arrow-shaped structures. The lower right panel shows the structures for the simulation conducted at *Wi*= 9, which marks the transition between the regimes of constant and increasing energy. As seen, arrow-shaped structures of moderately stretched polymers can already be identified at this *Wi* value. The largest *Wi* at which the ArrowRW state was found is *Wi*= 19. Above this value, the solution becomes unstable and the simulations converge to a stationary pattern of elastically induced vortices known as diwhirls (DW, brown line in figure 4 (b)). The dynamics of the DW have been recently shown in detail in [16] and thus will not be discussed here. Other solution branches, labeled as AArrowRW and DO in the figure, were also found at large *Wi* numbers and will be discussed in section 5.

All the arrow-shaped rotating waves found in this study propagate very slowly, with a rotation frequency (calculated from fast Fourier transform of a time series of the radial velocity) of the
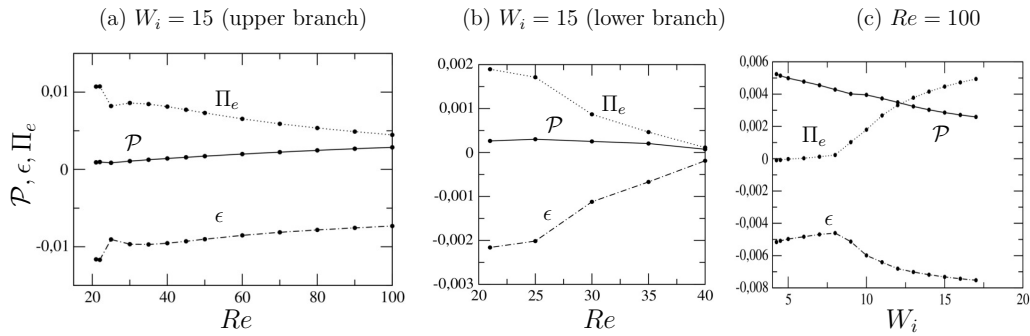
Page 29 of 34

Submitted to Phil. Trans. R. Soc. A - Issue

Figure 6. Variation of the inertial ($\mathcal{P}$), viscous (ϵ) and polymeric (Π_e) contributions to the integral energy balance (i.e. kinetic energy budgets) in (a) upper branch solution of the ArrowRW for $W_i = 15$, (b) lower branch solution of the ArrowRW for $W_i = 15$ and (c) ArrowRw for $Re = 100$ and varying W_i. In each panel, $\mathcal{P}$, ϵ and Π_e are shown as solid, dash-dotted and dotted lines, respectively.

order of $f \sim 10^{-3}(\Omega_i r_i)/d$. Moreover, it is observed that the rotation frequency decreases as *Re* or *Wi* increases.

We finally investigate the relationship between the changes observed in the volume averaged kinetic energy as *Re* and *Wi* are varied and the physical mechanisms governing the physics of this problem (i.e. inertial, viscous, and elastic effects). To that extent, we have calculated the inertial ($\mathcal{P}$), viscous (ϵ), and polymeric (Π_e) contributions to the integral energy balance of the ArrowRW solution. For viscoelastic flows, the integral energy balance reads [50],

$$\int_V \mathcal{P}dV - \int_V \epsilon dV - \int_V \Pi_e dV = 0, \tag{4.1}$$

and $\mathcal{P}$, ϵ and Π_e are calculated as,

$$\mathcal{P} = -\overline{u'v'}\frac{\partial \overline{v}}{\partial r} + \overline{u'v'}\frac{\overline{v}}{r}, \tag{4.2}$$

$$\epsilon = \frac{2\beta}{Re}\overline{S':S'}, \tag{4.3}$$

$$\Pi_e = \frac{1-\beta}{Re}\overline{S':T'}. \tag{4.4}$$

Here, the overline denotes mean quantities, $S' = (\nabla\mathbf{v}' + \nabla\mathbf{v}'^T)/2$ indicates the rate of strain tensor and the prime symbol denotes deviations of the velocity or polymer stress tensor from their mean values. It must be noted that $\mathcal{P}$ and ϵ always act as a source and a sink of energy, respectively. However, Π_e can be either a source or a sink depending on whether the sign of the integral is negative or positive (note that there is a minus sign in front of the integral). In panel (a) of figure 6, it is shown how the values of these three integrals (including the sign in front of them) vary with *Re* along the upper branch solution curve. As seen, for all *Re* numbers, the polymeric contribution is the dominant energy source (polymers are injecting energy into the flow), reflecting again the elastic nature of the ArrowRW solution. At the lowest values of *Re* (near the turning point), the contribution of Π_e is larger than that of $\mathcal{P}$ by two orders of magnitude. However, as *Re* increases, the contribution of $\mathcal{P}$ increases, and the contribution of Π_e decreases, so that at the largest *Re* values where the ArrowRW solution exists, they are similar in magnitude. This behaviour was expected, as in this analysis we keep $W_i = 15$, and so, as *Re* increases, the relative importance of inertial effects against elastic effects increases. In panel (b), the variation of the contributions of $\mathcal{P}$, ϵ, and Π_e is shown for the lower branch solution curve when $W_i = 15$. While the contribution of Π_e continues to be the dominant energy source near the turning point, its magnitude decays fast as *Re* increases and it becomes of the same order of magnitude as the inertial contribution at $Re \approx 30$. These analyses show that, at this *Wi* value,

12

steady ArrowRW states appear only when the flow is entirely dominated by elasticity, and that these solutions become unstable as the inertial effects become comparable to elastic effects. Finally, panel (c) of 6 illustrates the same analysis for the case in which $Re = 100$ and W_i is varied. It is observed that, at low Wi numbers, inertia is the dominant energy source. Although the net polymeric contribution at these Wi is positive and hence polymers also act as an energy source, its magnitude is very small when compared to the inertial contribution. Interestingly, this low contribution of the polymers to the integral energy balance persists until $Wi \approx 9$ is achieved, and it is thus consistent with the regime where the volume averaged kinetic energy is constant and stable forked-like structures are observed. Beyond this threshold, the contribution of Π_e grows quickly with increasing Wi, and this, along with the gradual decrease in the inertial contribution, results in a flow regime similar to that described in panel (a), where the polymeric contribution is the main energy source. It is when this happens that arrow-shaped structures of highly stretched polymers are observed.

5. Other solution branches

Having presented the ArrowRW solution in detail, we next focus on other solution branches where arrow-shaped structures of polymer stretch are also present. The first of these solutions, which has been dubbed asymmetric arrow rotating wave (AArrowRW), emerges at $Wi \approx 17.3$ (for $Re = 100$) when the ArrowRW undergoes a symmetry-breaking bifurcation that breaks the axial symmetry of the structures. This characteristic becomes clear when figure 7 (a), which illustrates the AArrowRW state at $Re = 100$ and $Wi = 18$, is compared with figure 1 (middle panels). Whereas for the ArrowRW, the arrow-shaped structures (including the wake) are symmetric with respect to the horizontal plane passing through the axis of the arrow, this symmetry is not preserved by the AArrowRW. In this latter state, there is an increase of the polymer stretch in the lower half of the structures (see that the colour intensity in this region right after the arrowhead is slightly darker than in the upper half), which results in the wake extending over a larger azimuthal distance than in the upper half. This asymmetry is, of course, also reflected in the structures of the radial velocity. By comparing the left and right panels in figure 7 (a), it can be seen that the increase in polymer stretch taking place in the lower half of the arrows is associated with shear layers that form in the boundaries between inflows and outflows. These shear layers are readily identified in the figure as regions where the contours of radial velocity are closely spaced, thereby indicating strong velocity gradients.

The AArrowRW is stable in a narrow range of Wi numbers, $17.3 \lesssim Wi \lesssim 18.4$ for $Re = 100$ (see blue diamonds in figure 4 (b)). Within this range, the symmetrically related state, AArrowRW* = K_zAArrowRW, has also been found (not shown). It has the same characteristics as the AArrowRW state, but shear layers and higher polymer stretch are in this case observed in the upper half of the arrow-shaped structures. It should also be noted that, unlike the ArrowRW state, the kinetic energy of the AArrowRW decreases monotonically as Wi increases. Following the solution beyond $Wi \gtrsim 18.4$, the flow becomes chaotic and the kinetic energy decreases markedly (see states denoted by (orange) cross marks in figure 4 (b)). Irregular arrow-shaped structures are transiently observed in the polymer stretch field, coexisting with strips of highly stretched polymers that extend over the entire azimuthal length (see figure 7 (b)). Unlike the flow states described above, arrow-shaped structures appear at random θ and z locations and their azimuthal extent is highly variable. Due to this randomness, the property that the structures are shifted by half a wavelength every half a rotation period is evidently absent. This chaotic flow is consistent with a state of disordered oscillations (DO), which is the term used in viscoelastic Taylor–Couette flow to denote chaotic flow patterns characterized by large-scale irregular flow structures [21,23–25,39]. This is, however, the first time that a DO state with arrow-shaped structures is reported.

Another flow state where arrow-shaped structures also appear is found at low Re values, near the saddle-node bifurcation point of the ArrowRW (see (red) squares in 4 (a)). Such state, which

Page 31 of 34

Submitted to Phil. Trans. R. Soc. A - Issue

13

is presented in figure 7 (c) for $Re= 30$ and $Wi= 15$, exhibits axially symmetric arrow-shaped structures of polymer stretch which are similar in length and magnitude to those of the ArrowRW. However, they appear only in one half of the system, i.e. over half a rotation period. We have dubbed this flow state as localised arrow shaped rotating wave (LArrowRW). We would like to note that localisation of structures in TCF usually happens in the axial direction or in both axial and azimuthal directions, resulting in patches. The azimuthal localisation observed in this viscoelastic flow state is thus quite unusual and the mechanism behind it is still not understood. The parameter range in which the LArrowRW state exists is smaller than that for the ArrowRW state, for both Re and Wi numbers (see (red) squares in figure 4). When $Wi= 15$, the minimum Re value up to which the LArrowRW can be followed is $Re\approx 16.5$, where the flow recovers its laminarity, whereas the highest Re value at which this state exists is $Re\approx 45$. Beyond this value, this solution branch becomes unstable and the simulations converge to the ArrowRW state. When the flow pattern is continued in Wi, while keeping $Re= 30$, the flow laminarises below $Wi\approx 11.5$. The kinetic energy of the LArrowRW increases monotonically with increasing Wi (states with nearly constant energy have not been found for this solution) until at $Wi\approx 23$, this solution loses stability to the ArrowRW.

Flow structures which do not exhibit arrow-shaped structures have also been found at low Wi numbers. These are well-known structures of TCF, the so-called spirals (SP) and ribbons (RB) states [3,12]. SP are found to exist when $0.5\lessapprox Wi\lessapprox 6.5$, whereas RB exist in a narrower region, $1.5\lesssim Wi\lesssim 3.5$ (see figure 4 (b)). These flow patterns have been widely analysed in the literature and will not be further discussed here.

6. Conclusion

Using direct numerical simulations of the governing equations, we have demonstrated the existence of axially localized, arrow-shaped structures of polymer stretch in the TCF of a dilute polymer solution. These structures have been identified in both rotating waves and in disordered flow patterns. An analysis of the integral energy balance has revealed that stable arrow-shaped rotating waves occur when the energy input associated with elastic mechanisms is the leading order term. In contrast, when the elastic and inertial contributions are comparable, these solutions become unstable.

Recently, arrow-shaped regions of highly stretched polymers have also been identified in viscoelastic channel flow at elasticity levels similar to those investigated here. Despite these structures being qualitatively distinct from those we report, it is interesting to note that in both cases they are aligned with the mean flow direction (the azimuthal direction in TCF and the axial direction in channels). This observation appears to support the hypothesis in [33] that arrow-shaped structures are caused by an increase in the elongational viscosity of the flow due to polymer stretching in the primary flow direction, and it suggests that they could exist in any viscoelastic fluid flow where there is a dominant velocity component.

Among the rotating waves found in the study, it is particularly interesting the LArrowRW state, where the arrow-shaped structures are only found in half of the system. Further research is needed to understand the mechanism behind this surprising feature. It also remains to see if these rotating waves persist in a real TCF system, where the assumption of axial periodicity adopted in our study is not fulfilled. Simulations with axial boundary conditions mimicking the experimental end-plates and/or laboratory experiments will be needed to answer this question. It should be noted that although the polymer stretch field cannot be easily measured in experiments, we have shown that another distinctive feature of these rotating waves is that the radial velocity structures are also arrow headed and point in the flow direction. Since the temporal evolution of the rotating wave pattern is equivalent to its azimuthal dependence, a space time plot of the radial velocity obtained at the mid-gap and at constant θ, over a rotation period, would be identical to
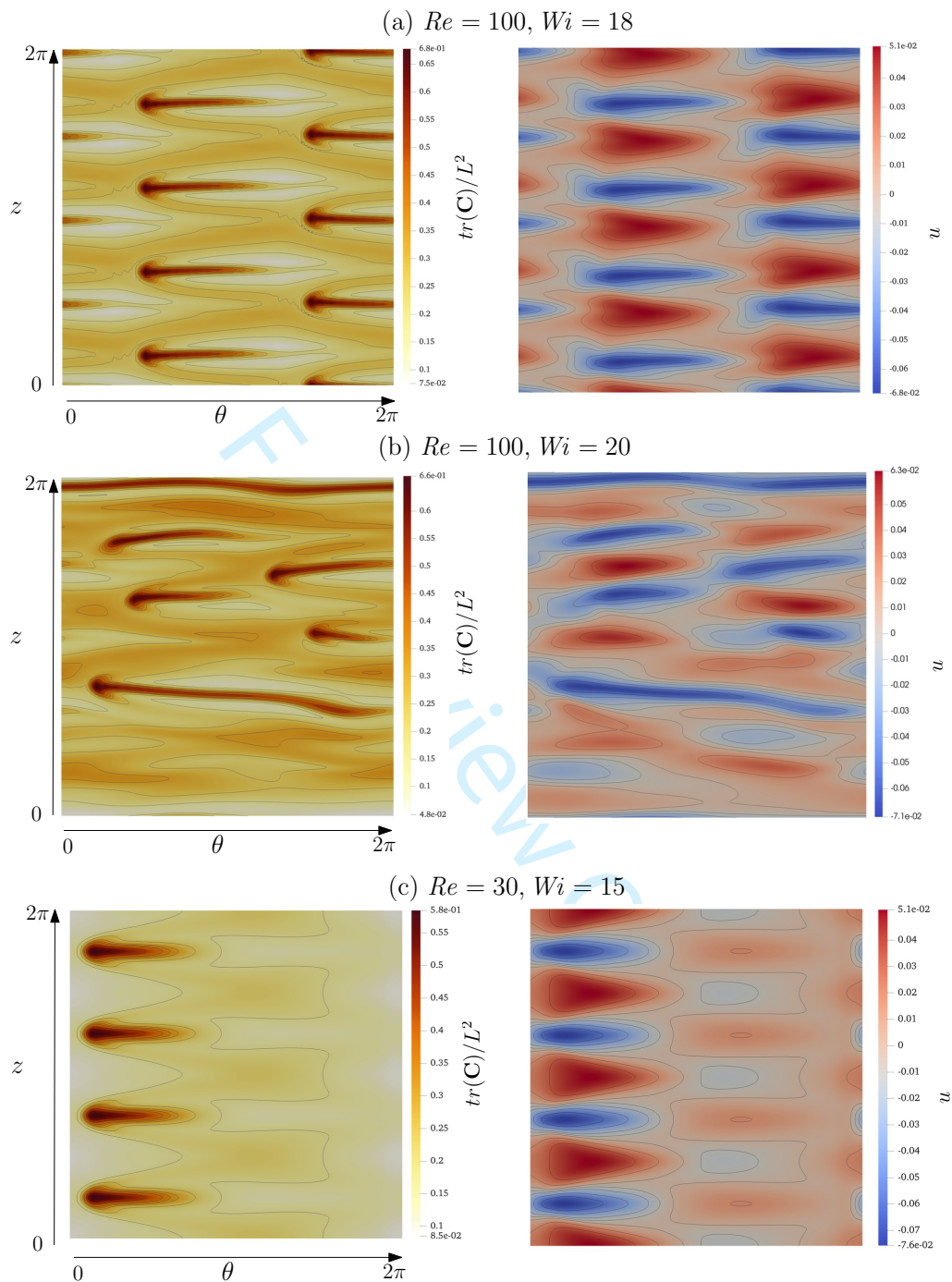
Figure 7. (Color online) Colour maps of the polymer stretch field (left panels) and radial velocity (right panels) illustrating other flow states where arrow-shaped structures of polymer stretch are also observed. (a) AArrowRW for $Re= 100$ and $Wi= 18$, (b) DO for $Re= 100$ and $Wi= 20$ and (c) LArrowRW for $Re= 30$, and $Wi= 15$. As in the previous figures, a cylindrical section (θ, z) obtained at the mid-gap is shown in each panel. Eight contours evenly spaced across the entire range of values (indicated in the colorbar) are shown in each case. The flow direction is from left to right.

the cylindrical sections presented in this paper. This characteristic could hence be used to detect these structures in experiments.

Despite its age and extensive research, the classical TCF setup (inner cylinder rotating and outer cylinder at rest) offers a great opportunity to detect previously unknown states. This is especially true when non-Newtonian fluids, such as viscoelastic fluids, are used as working fluids, further expanding the problem's already large parameter space.

References

1. Taylor, G. I. 1923. Stability of a viscous liquid contained between two rotating cylinders *Philos. Trans. R. Soc. Lond. A* **223** 289.
2. Andereck, C. D. Liu, S. S. and Swinney, H. L. 1986. Flow regimes in a circular Couette system with independently rotating cylinders. *J. Fluid Mech.* **164**, 155.
3. Chossat, P. & Iooss, G. 1994. *The Couette-Taylor Problem* Springer, Berlin.
4. Tagg, R. 1994. *The Couette-Taylor Problem* Nonlinear Sci. Today **4**, 1.
5. Langford, W. F., Tagg, R., Kostelich, E. J., Swinney, H. L. and Golubitsky, M. 1988. Primary instabilities and bicriticality in flow between counter rotating cylinders. *Phys. Fluids* **31**, 776-785.
6. Jones, C. A. 1981. Nonlinear Taylor vortices and their stability. *J. Fluid Mech.* **102**, 249âĂŞ261.
7. Jones, C. A. 1985. The transition to wavy Taylor vortices. *J. Fluid Mech.* **157**, 135âĂŞ162.
8. King, G. P., Lee, Y. Li, W., Swinney, H. L. and Marcus, P. S. 1984. Wave speeds in wavy Taylor-vortex flow. *J. Fluid Mech.* **141**, 365âĂŞ390.
9. Wereley, S. T. and Lueptow, R. M. 1998. Spatio-temporal character of non-wavy and wavy TaylorâĂŞCouette flow. *J. Fluid Mech.* **364**, 59âĂŞ80.
10. Martinand, D., Serre, E. and Lueptow, R. M. 2014. Mechanisms for the transition to waviness for Taylor vortices. *Phys. Fluids* **26**,(9), 094102.
11. Dessup, T., Tuckerman, L. S., Wesfreid, J. E., Barkley, D. and Willis, A. P. 2018. Self-sustaining process in Taylor-Couette flow. *Phys. Rev. Fluids* **3**, 123902.
12. Andereck, C. D., Liu, S. S. and Swinney, H. L. 1986. Flow regimes in a circular Couette system with independently rotating cylinders. *J. Fluid Mech.* **164**, 155-183.
13. Lacassagne, T., Cagney, N. and Balabani, S. 2021. Shear-thinning mediation of elasto-inertial TaylorâĂŞCouette flow. *J. Fluid Mech.* **915**, A91.
14. Lacassagne, T., Cagney, N., Gillissen, J. J. J. and Balabani, S. 2020. Vortex merging and splitting: A route to elastoinertial turbulence in Taylor-Couette flow. *Phys. Rev. Fluids* **5**, 113303.
15. Cagney, N., Lacassagne, T. and Balabani, S. 2020. TaylorâĂŞCouette flow of polymer solutions with shear-thinning and viscoelastic rheology. *J. Fluid Mech.* **905**, A28.
16. Lopez Jose. M. 2022. Vortex merging and splitting events in viscoelastic Taylor–Couette flow. *J. Fluid Mech.* **946**, A27.
17. Latrache, N. and Mutabazi, I. 2021. Transition to turbulence via flame patterns in viscoelastic TaylorâĂŞCouette flow. *Eur. Phys. J. E Soft Matter* **44** (5), 63.
18. Muller, S. J., Larson, R. G. and Shaqfeh, E. S. 1989. A purely elastic transition in Taylor-Couette flow. *Rheologica Acta* **28** (6), 499âĂŞ503.
19. Larson, R. G., Shaqfeh, E. S. G. and Muller, S. J. 1990. A purely elastic instability in TaylorâĂŞCouette flow. *Journal of Fluid Mechanics* **218**, 573âĂŞ600.
20. Shaqfeh, E. S. G. 1996 Purely elastic instabilities in viscometric flows. *Annu. Rev. Fluid Mech.* **28** (1), 129âĂŞ185.
21. Groisman, A. and Steinberg, V. 1996. Couette-Taylor flow in a dilute polymer solution. *Phys. Rev. Lett.* **77**, 1480âĂŞ1483.

Submitted to Phil. Trans. R. Soc. A - Issue

Page 34 of 34

22. Crumeyrolle, O., Mutabazi, I. and Grisel, M. 2002. Experimental study of inertioelastic CouetteâĂŞTaylor instability modes in dilute and semidilute polymer solutions. *Phys. Fluids* **14** (5), 1681âĂŞ1688.

23. Thomas, D. G., Khomami, B. and Sureshkumar, R. 2009. Nonlinear dynamics of viscoelastic TaylorâĂŞCouette flow: effect of elasticity on pattern selection, molecular conformation and drag. *J. Fluid Mech.* **620**, 353âĂŞ382.

24. Thomas, D. G., Sureshkumar, R. and Khomami, B. 2006. Pattern formation in Taylor-Couette flow of dilute polymer solutions: Dynamical simulations and mechanism. *Phys. Rev. Lett.* **97**, 054501.

25. Latrache, N., Abcha, N., Crumeyrolle, O. and Mutabazi, I. 2016. Defect-mediated turbu- lence in ribbons of viscoelastic Taylor-Couette flow. *Phys. Rev. E* **93**, 043126.

26. Groisman, A. and Steinberg, V. 1997. Solitary vortex pairs in viscoelastic Couette flow. *Phys. Rev. Lett.* **78**, 1460âĂŞ1463.

27. Baumert, B. M. and Muller, S. J. 1997. Flow regimes in model viscoelastic fluids in a circular Couette system with independently rotating cylinders. *Phys. Fluids* **9** (3), 566–586.

28. Baumert, B. M. and Muller, S. J. 1999. Axisymmetric and non-axisymmetric elastic and inertio-elastic instabilities in TaylorâĂŞCouette flow. *J. Nonnewton. Fluid Mech.* **83** (1), 33âĂŞ69.

29. Liu, N. and Khomami, B. 2013. Elastically induced turbulence in TaylorâĂŞCouette flow: direct numerical simulation and mechanistic insight. *J. Fluid Mech.* **737**, R4.

30. Song, J., Lin, F., Liu, N., Lu, X.-Y. and Khomami, B. 2021a. Direct numerical simulation of inertio-elastic turbulent TaylorâĂŞCouette flow. *J. Fluid Mech.* **926**, A37.

31. Song, J., Teng, H., Liu, N., Ding, H., Lu, X.-Y. Khomami, B. 2019 The correspondence between drag enhancement and vortical structures in turbulent TaylorâĂŞCouette flows with polymer additives: a study of curvature dependence. *J. Fluid Mech.* **881**, 602âĂŞ616.

32. Page, J., Dubief, Y. and Kerswell, R. R. 2020. Exact traveling wave solutions in viscoelastic channel flow. *Phys. Rev. Lett.* **125**, 154501.

33. Dubief, Y. and Page, J. and Kerswell, R. R. and Terrapon, V. E. and Steinberg, V. 2022. First coherent structure in elasto-inertial turbulence. *Phys. Rev. Fluids* **7** (7), 073301.

34. Samanta, D. Dubief, Y. Holzner, M. Schäfer, C. Morozov, A. N. *et al.* 2013. Elasto-inertial turbulence. *PNAS* **110**, 10557-62.

35. Dubief, Y. Terrapon, V. E. Soria, J. 2013. On the mechanism of elasto-inertial turbulence. *Phys. Fluids* **25** 110817.

36. Sid, S. Terrapon, V. E. Dubief Y. 2018. Two-dimensional dynamics of elasto-inertial turbulence and its role in polymer drag reduction. *Phys. Rev. Fluids* **3** 011301.

37. Shekar, A. McMullen, R. M. Wang, S. N. McKeon, B. J. Graham, M. D. 2019b. Critical-layer structures and mechanisms in elastoinertial turbulence. *Phys. Rev. Lett.* **122** 124503.

38. Bird, R., Dotson, P. and Johnson, N. 1980. Polymer solution rheology based on a finitely extensible beadâĂŤspring chain model. *J. Nonnewton. Fluid Mech.* **7** (2), 213 âĂŞ 235.

39. Liu, N. and Khomami, B. 2013. Elastically induced turbulence in TaylorâĂŞCouette flow: direct numerical simulation and mechanistic insight. *J. Fluid Mech.*, **737**, R4.

40. Song, J., Lin, F., Liu, N., Lu, X.-Y. and Khomami, B. 2021. Direct numerical simulation of inertio-elastic turbulent TaylorâĂŞCouette flow. *J. Fluid Mech.*, **926**, A37.

41. Song, J., Teng, H., Liu, N., Ding, H., Lu, X.-Y. and Khomami, B. 2019. The correspondence between drag enhancement and vortical structures in turbulent TaylorâĂŞCouette flows with polymer additives: a study of curvature dependence. *J. Fluid Mech.*, **881**,602âĂŞ616.

42. Song, J., Wan, Z.-H., Liu, N., Lu, X.-Y. and Khomami, B. 2021b. A reverse transition route from inertial to elasticity-dominated turbulence in viscoelastic TaylorâĂŞCouette flow. *J. Fluid Mech.* **927**, A10.

43. Lopez, J. M., Feldmann, D., Rampp, M., Vela-Martin, A., Shi, L. and Avila, M. 2020 nsCouetteâĂŞa high-performance code for direct numerical simulations of turbulent TaylorâĂŞ Couette flow. *SoftwareX* **11**, 100395.

44. Lopez, J. M., Choueiri, G. H. and Hof, B. 2019 Dynamics of viscoelastic pipe flow at low Reynolds numbers in the maximum drag reduction limit. *J. Fluid Mech.*, **874**, 699âĂŞ719.

45. Willis, A. P. 2017 The openpipeflow NavierâĂŞStokes solver. *SoftwareX* **6**, 124 âĂŞ 127.

46. Groisman, A. and Steinberg, V. 1998 Mechanism of elastic instability in Couette flow of polymer solutions: Experiment. *Phys. Fluids* **10** (10), 2451âĂŞ2463.

47. Buza, G., Page, J. and Kerswell, R. 2022. Weakly nonlinear analysis of the viscoelastic instability in channel flow for finite and vanishing Reynolds numbers. *J. Fluid Mech.*, 940, A11

Page 35 of 34

Submitted to Phil. Trans. R. Soc. A - Issue

48. Choueiri, G. H., Lopez, J. M., Varshney, A., Sankar, S. and Hof, B. 2021. Experimental observation of the origin and structure of elastoinertial turbulence. *Proc. Natl. Acad. Sci. U.S.A.*, **118** (45), e2102350118.

49. Itano, T. and Toh, S. 2001 The dynamics of bursting process in wall turbulence. *J. Phys. Soc. Japan* **70** (3), 703âĂŞ716.

50. Dallas, V. and Vassilicos, J. C. and Hewitt, G. F. 2010. Strong polymer-turbulence interactions in viscoelastic turbulent channel flow. *Physical Review E*, **82**, (6), 066303.

17